An enhanced k-ω SST model to predict airflows around isolated and urban buildings

Juan M. Gimenez[a,c], Facundo Bre[b,c]

[a] *Centre Internacional de Mètodes Numèrics en Enginyeria (CIMNE), Edifici C1 Campus Nord UPC C/ Gran Capità, S/N, Barcelona, 08034, Spain*
[b] *Institut für Werkstoffe im Bauwesen, Technische Universität Darmstadt, Franziska-Braun-Straße 3, Darmstadt, 64287, Germany*
[c] *Centro de Investigación de Métodos Computacionales (CIMEC UNL/CONICET), Col. RN 168, Km 0, Santa Fe, 3000, Argentina*

Abstract

The goal of this research is to improve and validate a Reynolds Averaged Navier-Stokes (RANS) turbulence model to perform accurate Computational Fluid Dynamics (CFD) simulations of the urban wind flow. The k-ω SST model is selected for calibration since its blended formulation holds remarkable optimization potential and has increased relevancy in recent studies in the field. A simulation-based optimization approach recalibrates the model closure constants by minimizing the prediction error of wind pressure coefficients on an isolated cubical building because this scenario contains many salient features observed in the flow in actual urban areas. The optimization procedure ensures both the coherence of calibrated model constants involved in the wall function formulations and the relationship between them to satisfy the flow horizontal homogeneity of the atmospheric boundary layer. The tuned closure coefficients increase momentum diffusion in the wake, resulting in shorter and more accurate predictions of the reattachment lengths. Validation case studies with wind tunnel measurement data from various urban scenarios were addressed to comprehensively assess the adaptability of the optimal set of coefficients reached. The results confirm that CFD predictions with the optimized model are consistently in closer agreement with experimental data than the standard version of k-ωSST. The root mean square errors are reduced by about 75% in pressure, 40% in velocity, and 20% in turbulent kinetic energy.

Keywords: Urban wind flow, RANS modeling, k-ω SST, Optimization, Turbulent flow, Wind pressure coefficients

1. Introduction

The increasing population and urbanization conduce to the conformation of large cities with high-density populated urban areas. The local atmospheric conditions impact the quality of life of urban residents because they affect building energy performance, thermal comfort, and human morbidity and mortality. Therefore, it is essential to investigate urban microclimates. Studies of the airflow field around

*Final publication available at: https://doi.org/10.1016/j.buildenv.2023.110321

buildings often use field measurements [1, 2] and reduced-scale wind tunnel experiments [3, 4]. As computational power becomes more cost-effective and available, computational fluid dynamics (CFD) simulations are increasingly applied to solve urban wind engineering problems. At the urban microscale, this technique enables the study of wind loads on buildings for structural analysis and natural ventilation design, pedestrian wind comfort, and air pollutant dispersion [5].

Given the complexity and the wide range of flow scales present in the turbulent atmospheric boundary layer (ABL) flow, the direct numerical solution of the governing equations is not affordable. Among the turbulence models employed, Large Eddy Simulation (LES) is intrinsically superior in terms of physical modeling to Reynolds-Average Navier Stokes (RANS) approaches. However, for most focus areas in urban physics, 3D steady RANS remains the primary CFD approach up to the present day [6, 7]. Many reasons justify the selection, such as the computational expense or the increased model complexity of LES, and the existence of best practice guidelines for RANS but not for LES [8–10]. Additionally, the use of hybrid LES and unsteady RANS (URANS) approaches is still limited in building simulation. Despite the promised balance of accuracy and computational cost, the border between the regions where URANS and LES are applied in urban airflow is usually ill-defined. Again, the lack of guidelines attempts against reliable predictions with this approach.

The time-averaged solutions yielded by RANS are valuable data for several practical ABL applications. Mean pressure coefficients are critical data for modeling natural ventilation in buildings, a key passive strategy for designing energy-efficient buildings, and improving indoor air quality [11]. The pedestrian discomfort criterion is based on gust speed, which is usually estimated from the mean wind speed and its standard deviation [12]. The transport of a passive or reactive scalar is usually incorporated to model the near-field pollution dispersion [13]. Moreover, steady RANS solutions have attracted renewed interest as an affordable data source for computationally expensive objectives, such as aerodynamic shape optimization [14, 15] or the construction of pedestrian wind comfort maps of neighborhoods [16].

The efficacy of these applications is contingent upon the dependability of RANS solutions, which are known to have issues in modeling flow around bluff bodies. On the CFD results of complex urban environments, the turbulence models impact more than other modeling aspects, such as the imposed roughness on the ground and walls [17]. The development of specific models improves the estimation of turbulent kinetic energy (TKE) in the impinging region of building walls [18, 19], but their use is limited because these enhancements were found to be less significant in other scenarios. The renormalization group k-ϵ (RNG) and the k-ω with shear stress transport (k-ω SST) models alleviate the pressure overestimation in the stagnation zone on the windward building surface. These models have shown satisfactory agreement with experimental data and are currently recommended for ABL applications [20–22]. In this context, a trend in the most recent literature suggests that the k-ω SST model is gaining relevance for the study of urban wind flows [23–25]. Anyhow, the inaccurate prediction of flow separation and reattachment is a recognized drawback of any steady RANS two-equation model. This issue leads to a poor estimation

of the airflow in the wake region behind bodies and the subsequent inaccuracy of the predicted pressure on lateral and leeward surfaces [11, 24, 26, 27]. These limitations of RANS models are highlighted in sheltered conditions such as actual urban areas because buildings downstream from each other are the norm [21, 28].

Predictions based on RANS turbulence modeling are hindered by structural and parametric uncertainties. While the structural ones are related to the modeling hypothesis as the Boussinesq approximation, the parametric ones arise from the semi-empirical closure coefficients embedded in the transport equations [29, 30]. These latter were primarily calibrated to match specific physical problems with experimental data, such as homogeneous decaying turbulence, free shear flow, and fully developed channel flow, among others. Such flows have limited similarities with the airflow characteristics around buildings in the ABL. Even though the authors of the models provided standard values for the flows they investigated, CFD practitioners use these standard coefficients regardless of whether they are fit to properly describe the problem under analysis.

Because of the inherent uncertainties in the value of the closure coefficients of RANS turbulence models, some research considered recalibrating them to represent specific flows of interest. The reattachment point in the backward-facing step flow was the target to calibrate diverse RANS models using different techniques, such as genetic algorithms (GA) [31] and genetic programming [32]. In Ref. [33], the calibration of the closure coefficients of the Spalart–Allmaras turbulence model was carried out using machine learning for a transonic wall-bounded flow around an airfoil. The uncertainty of closure coefficients and their adjustment for transitional flows were studied in Ref. [34]. The k-ω SST model was calibrated for free surface flows on slopes using machine learning techniques in Ref. [35]. Neural networks were employed to improve the prediction of the k-ω model for the flow separation in a periodic hill in Ref. [36].

Regarding ABL applications, a Bayesian-based recalibration of the standard k-ϵ closure coefficients was addressed for the particular case study of a flow over a street canyon using TKE measurements as reference data [37]. Ref. [38] summarized several case studies where stochastic optimization was applied to calibrate RANS models for different urban configurations. This study proved the need to find a set of customized closure coefficients for RANS turbulence models suitable for a wide range of urban flow problems. Ref. [39] introduced a simulation-based optimization method based on a dynamic coupling of CFD simulations and GA. That approach improves the prediction of wind surface-averaged pressure coefficients on a wide range of isolated low-rise buildings using RNG k-ϵ and Spalart-Allmaras models, which reduced the root mean square error (RMSE) by 64% in unseen flow scenarios. In Ref. [40] several k-ϵ based turbulence models were calibrated prioritizing the reproduction of the reattachment lengths in a single-building model. The generalizability of these models calibrated with the single-building was found to have limited performance for multi-building configurations. The calibrated models predicted with acceptable agreement only the TKE at ground level but overestimated the TKE in the upper regions. Although this study provided important advances, there is no mention of whether the coefficients involved

in the wall functions models were also calibrated, which could explain these deviations. Overall, it is not possible to guarantee that previous investigations simultaneously assure the coherence of calibrated model constants involved in the wall function formulations and the relationship between these model constants that satisfies the horizontal homogeneity of the ABL profile.

In the reviewed current literature, no study has consistently enhanced the performance of RANS models, via its recalibration, to predict airflows around both isolated and urban buildings. This limitation is probably because no research has considered the restriction for the horizontal homogeneity of the ABL, which can impair the recalibration process by not guaranteeing that the modeled wind profile approaching the buildings match the one measured in the wind tunnel experiments. The current literature also indicates that the standard version of the k-ω SST model is the most suited RANS model for urban airflow modeling, but no work has addressed its recalibration for this application. Therefore, this research aims to optimize the constants of the k-ω SST turbulence model to enhance the prediction of urban wind flow while satisfying the constraints in the numerical modeling of ABL. A bio-inspired simulation-based approach fits the model constants by predicting the mean pressure field on an isolated cubical building. Various urban case studies with experimental data are employed to comprehensively assess the generalizability of the optimal set of coefficients obtained. The prediction accuracy of relevant features of the urban flow is discussed through the analysis of mean pressure on building surfaces, and the mean velocities and turbulent kinetic energy fields near the buildings.

In the remainder of this paper, Section 2 describes the methodology to optimize the turbulence model and the comprehensive set of case studies selected to validate it. Section 3 presents the results of the optimization process and the exhaustive assessment of its accuracy in the computational study of wind flow in urban environments. Section 4 discusses the achievements and poses suggestions for future research. Finally, Section 5 concludes the work.

2. Methodology

This section introduces the methods used to develop and validate an optimized k-ω SST turbulence model suitable for the accurate computational study of wind flow in urban environments. Figure 1 presents the workflow where two main stages are devised. First, a bio-inspired optimization process based on genetic algorithms coupled with CFD simulations calibrates the closure constants of the standard k-ω SST model to enhance the prediction of pressure coefficients on building surfaces for a given *training* case. Second, the performance of the optimized model is validated in urban environments for three case studies selected from the bibliography. In this sense, the CFD results are compared with measurements from wind tunnel experiments considering not only pressure coefficients on target buildings but also specific features of the urban boundary layer as the turbulent flow at the pedestrian level.

The following subsections present the mathematical formulation, specifications of the methods used, selected case studies, and metrics for quantifying the deviations between numerical predictions and ex-

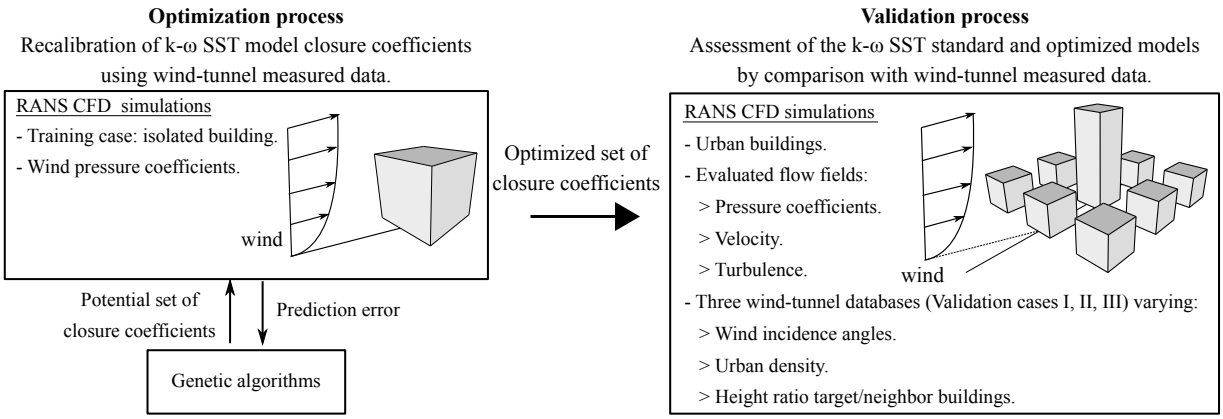

Figure 1: Scheme of the proposed methodology.

perimental results.

2.1. RANS equations and turbulence modeling

Incompressible homogeneous viscous fluid flow with constant density ρ and kinematic viscosity ν is considered. Decomposing the unknowns of the Navier-Stokes equations, velocity u_i and pressure p, into the sum of the mean value (time-averaged or ensemble-averaged) and fluctuating parts as $u_i = U_i + u_i'$ and $p = P + p'$, and averaging, leads to the Reynolds Averaged Navier-Stokes (RANS) equations, which are described as:

$$\frac{\partial U_i}{\partial x_i} = 0, \tag{1}$$

$$\frac{\partial U_i}{\partial t} + U_j \frac{\partial U_i}{\partial x_j} = -\frac{1}{\rho}\nabla P + \frac{\partial}{\partial x_j}\tau_{ij} - \frac{\partial}{\partial x_j}\left(u_i' u_j'\right). \tag{2}$$

where $\tau_{ij} = \nu\left(\frac{\partial U_i}{\partial x_j} + \frac{\partial U_j}{\partial x_i}\right)$.

Most RANS models assume that the fluctuating part u_i' obeys the Boussinesq hypothesis, such that,

$$-\frac{\partial}{\partial x_j}\left(u_i' u_j'\right) = \nu_t\left(\frac{\partial U_i}{\partial x_j} + \frac{\partial U_j}{\partial x_i}\right) - \frac{2}{3}k\delta_{ij}, \tag{3}$$

where ν_t is the kinematic eddy viscosity, and $k = \frac{1}{2}u_i' u_i'$ is the turbulent kinetic energy. The last term in Equation (3) guarantees equality when both sides are contracted (the two sets of indices are set equal and summed over). The RANS turbulence models can be grouped according to the number of additional transport equations required to estimate ν_t. The two-equation models (k-ϵ and k-ω families) have become industry standard and are commonly used for most types of engineering problems. The first variable, k, determines the energy in the turbulence, whereas the second variable determines the scale of the turbulence (length-scale ϵ or time-scale ω). In terms of modeling, probably the most flexible two-equation approach is the baseline model (BSL) introduced by Menter [41]. In this model, the blended formulation alleviates the near-wall dependency of k-ϵ models and the excessive sensitivity of the standard k-ω to the freestream

values. The BSL formulation combines the standard k-ω equations multiplied by a blending function F_1, and the transformed k-ϵ equations multiplied by $(1 - F_1)$ as:

$$\frac{\partial k}{\partial t} + U_j \frac{\partial k}{\partial x_j} = P - \beta^* k\omega + \frac{\partial}{\partial x_j}\left[(\nu + \alpha_k \nu_t)\frac{\partial k}{\partial x_j}\right], \tag{4}$$

$$\frac{\partial \omega}{\partial t} + U_j \frac{\partial \omega}{\partial x_j} = \frac{\gamma}{\nu_t} P - \beta \omega^2 + \frac{\partial}{\partial x_j}\left[(\nu + \alpha_\omega \nu_t)\frac{\partial \omega}{\partial x_j}\right] + 2(1 - F_1)\alpha_{\omega_2}\frac{1}{\omega}\frac{\partial k}{\partial x_i}\frac{\partial \omega}{\partial x_i}. \tag{5}$$

The k-ω SST model consists of adding to BSL formulation the additional capability to represent the transport of the principal shear stress in adverse pressure gradient boundary layers. The effect in the formulation is a modification of the value for some model closure coefficients, and the definition of the eddy viscosity. Other minor variations have been developed to improve the prediction of specific flows. According to the SST-2003m model [42], the production term is approximated by $P = \min\left(\nu_t S^2, c_1 \beta^* \omega k\right)$. Thus, the eddy viscosity is defined as:

$$\nu_t = \frac{a_1 k}{\max(a_1 \omega, b_1 S F_2)} \tag{6}$$

where $S = \sqrt{2 S_{ij} S_{ij}}$ is the strain invariant, with $S_{ij} = \frac{1}{2}\left(\frac{\partial U_i}{\partial x_j} + \frac{\partial U_j}{\partial x_i}\right)$.

Each of the constants is a blend of an inner (subindex 1) and outer (subindex 2) constant, which are blended via:

$$\psi = F_1 \psi_1 + (1 - F_1)\psi_2. \tag{7}$$

Additional functions are given by:

$$F_1 = \tanh(arg_1^4); \quad arg_1 = \min\left[\max\left(\frac{\sqrt{k}}{\beta^* \omega y}, \frac{500\nu}{y^2 \omega}\right), \frac{4\sigma_{\omega_2} k}{\mathrm{CD}_{k\omega} y^2}\right] \tag{8a}$$

$$\mathrm{CD}_{k\omega} = \max\left(2\sigma_{\omega_2}\frac{1}{\omega}\frac{\partial k}{\partial x_i}\frac{\partial \omega}{\partial x_i}, 10^{-10}\right) \tag{8b}$$

$$F_2 = \tanh(arg_2^2); \quad arg_2 = \max\left(2\frac{\sqrt{k}}{\beta^* \omega y}, \frac{500\nu}{y^2 \omega}\right) \tag{8c}$$

where y is the distance from the cell center to the nearest wall, and $\Omega = \sqrt{2 W_{ij} W_{ij}}$ is the vorticity magnitude, with $W_{ij} = \frac{1}{2}\left(\frac{\partial U_i}{\partial x_j} - \frac{\partial U_j}{\partial x_i}\right)$

The standard constants, presented in Table 1, were inherited from the original models. The key of the formulation is the blending function F_1. This gradually switches from the k-ω model in the sub- and log-layer to the k-ϵ model in the wake region of the boundary layer and free shear layers. Although this calibration has shown acceptable confidence in solving specific flows, the performance of the formulation to model flow around bluff bodies is herein investigated, as this type of scenario was not considered in the model's adjustment. Apparently, the blended formulation holds remarkable optimization potential by implicitly allowing calibration of the boundary between the inner and outer layers, and the sets of coefficients to be used in each region.

The k-ω SST model is showing increased relevance in the study of urban wind flows in the latest years. The current results indicate that the standard version of the k-ω SST model is the most suited RANS

model for urban airflow modeling, but still leaves room for improvements. This trend also supports the choice of the k-ω SST turbulence model for the optimization in this work.

Table 1: Closure coefficients in the k-ω SST model. Standard values and lower and upper limits for their calibration.

	β^*	α_{k_1}	α_{k_2}	α_{ω_1}	α_{ω_2}	β_1	β_2	γ_1	γ_2	a_1	b_1	c_1
standard	0.09	0.85	1.0	0.5	0.856	0.075	0.0828	5/9	0.44	0.31	1.0	10.0
lower limit	0.005	0.05	0.05	0.05	0.05	0.005	0.005	-	-	0.005	0.005	0.1
upper limit	1.0	5.0	5.0	5.0	5.0	2.0	2.0	-	-	2.0	2.0	20

2.2. Horizontally homogeneous atmospheric boundary layer flow

The lowest part of the atmospheric boundary layer can be considered fully aerodynamically rough, relatively free from any pressure gradient and horizontally homogeneous (HHABL) [43]. This property, which can only exist in regions remote from any obstructions, implies that the streamwise gradients of all variables should be zero. Since the pressure is constant, the flow is driven by a shear stress at the upper surface of the layer, and this is constant through the layer, equaling the shear stress at the wall.

The HHABL conditions are used to derive inlet profiles for the velocity and the turbulent variables from the conservation and equilibrium equations associated with particular turbulence models. Solutions of Equations (4) and (5) are essentially the same as presented in Ref. [44] for the k-ϵ model, and yield the same profile for U, it is:

$$U = \frac{u_*}{\kappa} \ln\left(\frac{z + z_0}{z_0}\right), \tag{9}$$

where u_* is the friction velocity, $\kappa = 0.4$ is the von Karman's constant, and z is the vertical coordinate (m). Because HHABL is considered, the friction velocity is constant along the height z and it can be calculated from a known velocity U_h at a reference height $z = h$ as:

$$u_* = \kappa \frac{U_h}{\ln\left((h + z_0)/z_0\right)}. \tag{10}$$

The value of the aerodynamic roughness height z_0 (m) usually follows the roughness classification proposed in Ref. [45]. The turbulent kinetic energy and specific dissipation rate (ω) inlet profiles are defined as:

$$k = \frac{u_*^2}{\sqrt{\beta^*}}, \qquad \omega = \frac{u_*}{\kappa \beta^* (z + z_0)}. \tag{11}$$

There is one constraint imposed in the solutions given by (9) and (11), namely, a unique relationship exists between the implied value of Karman's constant and the various closure coefficients. Specifically, the following restrictions must hold [46]:

$$\gamma_1 = \frac{\beta_1}{\beta^*} - \frac{\sigma_{\omega 1} \kappa^2}{\sqrt{\beta^*}} \tag{12a}$$

$$\gamma_2 = \frac{\beta_2}{\beta^*} - \frac{\sigma_{\omega 2}\kappa^2}{\sqrt{\beta^*}}. \tag{12b}$$

The ABL inhomogeneity, which refers to an unintended mismatch between the inlet and incident ABL profiles, can be a significant source of error and may compromise the reliability of flow predictions, e.g., pedestrian wind comfort [47] and wind loads [48]. Thus, preserving the wind profile is essential when wind tunnel data is used for calibration and validation purposes to avoid uncertainties regarding mismatching the incident profile.

To guarantee that the inflow ABL profile imposed preserves its shape throughout the upstream domain despite the distance from the inlet to the building the flow must be driven by a shear stress at the top boundary as $\tau_{top} = \rho u_*^2$. This condition must be employed along with a compatible wall function on the ground [49].

Regarding building surfaces, these are considered smooth surfaces, and a non-slip condition for the velocity is imposed on them. For turbulent variables, an automatic near-wall treatment shifts gradually between the viscous and logarithmic sub-layer formulations, based on the mesh density [50]. The use of such an approach alleviates the requirement of limiting the dimensionless wall distance (y^+) value at the first cell center from the wall in a pre-specified range, which is challenging to achieve with every cell on the wall, especially when addressing complex geometries.

Note that the wall functions used on the building surfaces and ground depend on several of the model closure coefficients, which are listed in Table 1. Thus, the calibration procedure herein proposed ensures consistency in the specification of these constants; i.e., the same value of each coefficient is employed for the transport equations of the turbulent variables, the definition of the ABL flow in the inlet, and the ground and wall functions.

2.3. CFD simulations

In this study, the cloud-based platform CpSimulator [21] is selected as the CFD tool. The platform comprises a set of tools to automate the entire workflow of ABL simulations and obtain detailed wind flow data around buildings in urban scenarios. These implementations include the generation of the computational domain, the meshing procedure, the solution stage, and the post-processing of the results.

The platform processes the geometric data of the scenario (the target building and its surrounding environment, if any) and reconstructs this information in a computational domain. This latter is a regular polygon whose dimensions met the ones advised by best practice guidelines [8] regarding the minimum distances between the building or urban model and the boundaries of the domain and the maximum allowed blockage ratio. Regarding discretization, the automatic evaluation of the reference cell size, DX, according to the whole dimensions of the buildings and the detection of characteristic lengths of each surface are key to guaranteeing a proper level of mesh refinement. A background mesh of cubical cells of size DX is recursively refined to shape the input surfaces that define the buildings and the boundaries of

the computational domain. Due to the recursive nature of the refinement process, i.e., splitting each cell into eight of half-length, the refinement ratio is two between refinement regions. The process preserves the aspect ratio, except near building surfaces, where prismatic layers are placed to guarantee that grid lines are perpendicular to the walls. The mesh quality is controlled via the maximum skewness, maximum non-orthogonality, and the number of undetermined cells, resulting in a proper discretization for the finite volume method [51]. The mesher prioritizes the quality requirements over a strict conforming of any detail of the geometry. The tool demonstrated great robustness due to, in most cases, and despite the complexity of the analyzed case, the automatic procedure achieves meshes with a large percentage of hexahedral cells, favoring the quality of the numerical solution obtained [21, 52].

The time-averaged RANS equations are solved using an implicit, segregated, three-dimensional finite volume method (FVM). Pressure-velocity coupling is solved with the SIMPLE algorithm by using the implementation available in the open-source software OpenFOAM. The running procedure starts the simulation with velocity and turbulent fields initialized everywhere to the inlet conditions. The relaxation used in initial iterations is gradually deactivated and discretization schemes are switched from first to second-order. The iterative solving process continues until the normalized residuals for pressure, velocity components, and turbulent fields have decreased by five orders of magnitude for each one. It should be emphasized that the RANS equations yield time-averaged solutions. Pressure, velocity, and turbulent kinetic energy will henceforth refer to these mean fields.

The requirements of the current study led to the development of new capabilities for the post-processing module. These allow the automatic sampling of solution fields on a list of measurement points given as input. Added functionalities enable the acquisition of pressure data on the surfaces, or velocity and turbulent kinetic energy data on specific locations around buildings. In particular, the wind pressure coefficient C_p at a point x_i on the façade is defined as,

$$C_p(x_i) = \frac{P(x_i) - P_\infty}{\frac{1}{2}\rho U_H^2}, \tag{13}$$

where $P(x_i)$ is the static pressure at the given point and P_∞ is the static reference pressure at far away from any disturbance. Finally, the surface-averaged pressure coefficient on a given surface of the building of area Ω is obtained as:

$$\overline{C_p} = \frac{1}{\Omega}\int_\Omega C_p \; d\Omega. \tag{14}$$

2.4. Optimization procedure

The calibration of the k-ω SST model can be addressed as an optimization problem which is defined as the searching of a set of closure coefficients $\mathbf{x} = (x_1, x_2, \ldots, x_n)$ that minimize the prediction error of CFD simulations regarding a given reference data, it is:

$$\min f(\mathbf{x}) \quad \text{subject to: } x_i^L \leq x_i \leq x_i^U, \; i = 1, \ldots, n \tag{15}$$

where x_i^L and x_i^U are the lower and upper limits for the design variable x_i. The objective function f is defined as

$$f(\mathbf{x}) = \frac{\text{RMSE}(\mathbf{x})}{\text{RMSE}(\mathbf{x}^0)} + \mathcal{R}, \tag{16}$$

where RMSE$(\cdot)$ is the root-mean-square error of the CFD simulations for the training case (see next section), and $\mathbf{x}^0$ and $\mathbf{x}$ are the standard and the modified set of closure coefficients, respectively. The second term ($\mathcal{R}$), serves to penalize solutions conducting to not-converged simulations since it increases the objective function proportionally to the unsatisfied residual convergence of the pressure equation. Thus, the term $\mathcal{R}$ is defined as:

$$\mathcal{R} = 0.1(\log_{10}(\max(r^*, r(\mathbf{x}))) - \log_{10}(r^*))^2 \tag{17}$$

where $r(\mathbf{x})$ is the last residual for the pressure equation system in the steady simulation and $r^* = 10^{-4}$ is the minimal convergence required for the residuals. Note that $\mathcal{R} = 0$ for converged simulations.

As to the lower and upper limits of the variables x_i^L and x_i^U of the k-ω SST model, there are no physical-based limits determined in the original work [41]. As described previously, the physical modeling of turbulence generation or dissipation is performed by including production and destruction terms, whose magnitudes are directly or indirectly modified through the closure coefficients. Therefore, the search range is expanded as much as is computationally possible, while considering mathematical restrictions (some of them cannot be zero) and their physical meaning (most of the coefficients must be positive). Moreover, restrictions expressed in Equation (12), which define γ_1 and γ_2 in terms of the remaining constants, are employed to guarantee the HHABL condition. Thus, these two coefficients are not included in the calibration procedure. Table 1 shows the limits adopted for each optimization variable.

To solve the single-objective optimization problem (15), and in agreement with the previous work of the authors [39], genetic algorithms (GA) are used. This bioinspired approach obtains better solutions than traditional gradient-based methods of optimization when functions with multiple local optima are evaluated. GA have low sensitivity to discontinuities in the objective function, and they are well-suited for parallel computing.

The chromosome of each individual of the population consists of a sequence of real numbers coding the modified constants of the k-ω SST model. The GA-based procedure comprises successive generations evaluating the fitness of each individual, which starts with a random population. A CFD simulation using the given set of coefficients is solved for the training case, and the Equation (16) determines a unique qualification of the aptitude, i.e. the fitness, of the evaluated individual. Then, the population of the following generation is getting using selection, crossover, and mutation operators that favor the fittest individuals. Iteration continues until a maximum number of generations is satisfied or a specified minimum fitness is reached. At this point, the fittest individual is considered the optimum. The description of the implementation and execution of the optimization procedure does not substantially differ from what is detailed in Ref. [39].

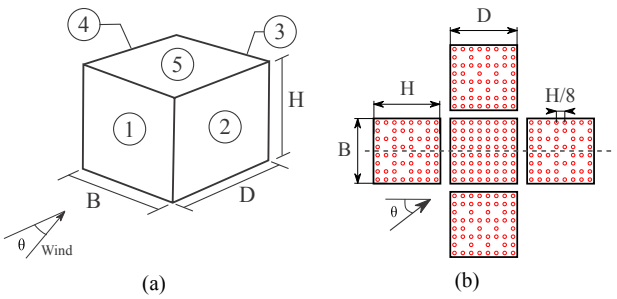

Figure 2: Case study for training. (a) geometry, wind incidence angle reference, and labeling of the building surfaces. (b) location of the measurement points.

2.5. Case study for training

In urban environments, the ABL wind-flow pattern is very complex. However, the flow around a simple isolated cubic building model contains many of the salient features that are also present in urban airflows [53]. The focus on this simple scenario has allowed researchers to clearly identify the main limitation of standard RANS models, the inability to accurately reproduce the flow separations and downstream flow field of the windward façade.

The potential room for improvement in this simple case is investigated through the recalibration of the k-ω SST model, presuming that an enhancement in the prediction accuracy for this case study could also improve the accuracy for multi-building configurations, such as urban environments. Under this assumption, the *training* case for the optimization procedure is selected from the database for isolated low-rise buildings of the Wind Engineering Information Center of the Tokyo Polytechnic University (TPU) [54]. In particular, the flat-roofed case with height-to-breadth (H/B) and depth-to-breadth (D/B) ratios of H/B=D/B=1 is selected. The experimental scale of 1/100 leads to H=B=D=0.1 m. The geometry configuration is displayed in Figure 2a.

A log-law profile adjusts the incident wind profile used in experiments with $U_h = 7.95$ m/s, $h = 0.16$ m, and $z_0 = 2 \times 10^{-4}$ m. Although wind tunnel data for wind incidence angles from 0° to 90° in 15° increments are available, only the case with 0° wind is taken.

The experimental data consists of a time series of the sampling of pressure coefficients at different locations on the roof and building surfaces, presented in Figure 2b. To be used as a reference solution in the optimization procedure, the data is pre-processed. First, a time average of the signal from each sensor is performed, obtaining a time-averaged value of the pressure coefficient at each measurement point. When analyzing these data, unexpected characteristics are observed, such as the lack of symmetry with respect to the axis of the selected wind incidence, marked by the dashed line in Figure 2b. One possible reason for this deficiency is having averaged a scarce time-series signal. To reduce this uncertainty, we have processed the data to impose proper symmetry conditions, resulting in the value of C_p at each measurement point being the average between itself and its symmetric.

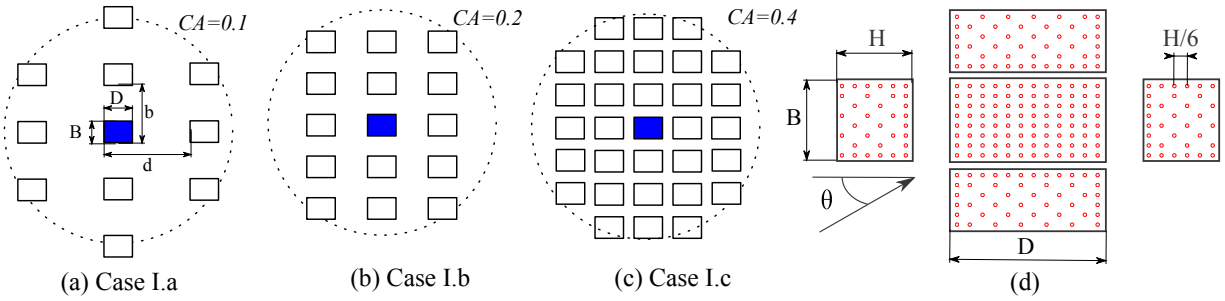

Figure 3: Validation Case I. Urban area for (a) Case I.a, (b) Case I.b, and (c) Case I.c. In (d) the location of the measurement points on the target building is presented.

2.6. Case studies for validation in urban environments

The use of the optimized model to predict flow in scenarios for which it was not trained must be validated. In particular, we are interested in evaluating the adaptability of the model in urban case studies. For this, three bibliographical references to wind tunnel tests for different geometries of urban prototypes are selected. Measurements of flow characteristics, such as pressure, velocity, and turbulence fields, provide an exhaustive data set to assess the model. These multi-building scenarios, which consider regular building topologies and structured arrangements, examine various levels of clustering between buildings and relative heights between the target building and its neighborhood.

Validation Case I. This multi-building case study and its experimental results are taken from the TPU database [54]. The so-called *target* building is a flat-roofed building with ratios of D/B = 3/2 and H/B = 1/2, see Figure 3(a). Real-scale sizes are B = 16 m, D = 24 m, and H = 12 m, with an experimental scale of 1:100. To measure wind pressures, over 256 taps were placed uniformly over the surfaces of the target building. The same geometry configuration is employed for the surrounding buildings, which are in a regular arrangement with different levels of clustering; see Figures 3(a)-(c). The area density CA is defined as:

$$\mathrm{CA} = \frac{\text{area occupied by buildings}}{\text{area of site}} = \frac{\mathrm{BD}}{\mathrm{bd}} \tag{18}$$

where b and d are the average distances between corresponding points on adjacent buildings in the two coordinate directions, as shown in Figure 3(d). The experiments with CA=0.1, 0.2 and 0.4 are taken for validation. This enables studying the sensitivity to the flow regime in the urban boundary layer [55]. The isolated roughness flow regime is analyzed with CA=0.4 (Case I.a), the wake interference flow with CA=0.2 (Case I.b), and the skimming flow with CA=0.1 (Case I.c).

A log-law profile adjusts the incident wind profile used in experiments with $U_h = 7.91$ m/s, $H = h =$ 0.12 m, and $z_0 = 1.5 \times 10^{-4}$ m. To compute C_p values an undisturbed pressure P=0 is considered. Wind pressure time series for wind incidence angles from 0° to 90° in 22.5° increments are used. The locations of the measurement points are shown in Figure 3(d). The time-averaged wind pressure coefficients are computed and stored as reference data.

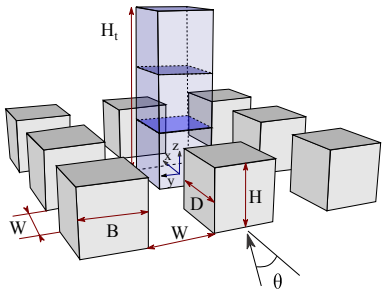

(a) Geometry Cases II and III

	II.a	II.b	II.c	III.a	III.b
B		0.2 m		0.1 m	
D		0.2 m		0.1 m	
H		0.2 m		0.1 m	
H_t	0H	1H	2H	1H	3H
W		0.2 m		0.1 m	
θ		0º, 22.5º, 45º		0º	

(b) Configurations

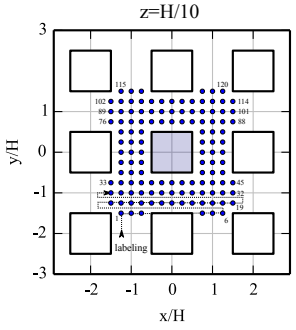

(c) Measurement points Case II

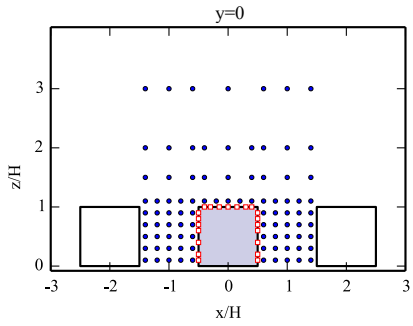

(d) Measurement points Case III.a

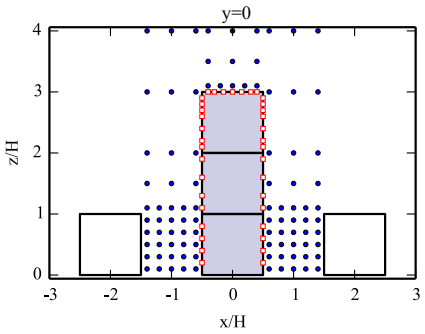

(e) Measurement points Case III.b

Figure 4: Validation Cases II and III. (a) Urban area for both cases. (b) geometry configurations, (c),(d) and (e) location of the measurement points, where empty-red and filled-blue markers represent pressure and velocity sensors, respectively.

Validation Case II. In this second validation case, the experimental results of the so-called *case C* from the Architectural Institute of Japan (AIJ) are used [9]. The database provides data from 9 experiments, 0°, 22.5°, and 45° for three different geometries. The geometries represent a small block of buildings, where there is no building at its center (H_t=0, Case II.a), a low-rise building at its center (H_t=H, Case II.b), and a high-rise building at its center (H_t=2H, Case II.c), see Figure 4(a). The surrounding cubic buildings are arranged in a regular form with a planar area density of CA=0.25. The configurations of the models are presented in Figure 4(b). A log-law profile with $U_H = 3.75$ m/s and $z_0 = 4.75 \times 10^{-4}$ m fits the approaching flow used in the wind tunnel experiments.

The wind tunnel experiment was thought to help validate the accuracy of CFD codes for pedestrian wind comfort assessments. In this context, the data provided consists of a set of time-averaged velocities on 120 measurement points located at a height of H/10, see Figure 4(c). We have labeled the sampling points following an increasing order along the canyons between buildings, which simplifies the analysis.

Validation Case III. This case study is based on the wind tunnel results reported in Ref. [56] whose data is made available in Ref. [57]. In that experiment, very close to test case C of the AIJ benchmark, a regular arrangement of nine cubic generic buildings with a planar area density of 0.25 was used. The height of the surrounding buildings was H = 0.1 m, whereas two different heights of 1 H and 3 H were considered for the target building, here namely Case III.b and Case III.b, respectively.

The case studied considers wind direction perpendicular to the building façades. Figures 4(a) and 4(b) introduces the scenario's geometry and its configuration. The mean approach velocity used in the experiments can be fitted to a log-law with a reference velocity $U_H = 3.02$ m/s and an aerodynamic roughness of $z_0 = 2 \times 10^{-4}$. After statistical analysis, mean velocities and turbulent kinetic energy (TKE) were reported on 90 and 95 measurement points over the central vertical plane in Cases III.a and III.b. The pressure on the façades was measured along the centerline of the target building at 21 and 37 points in Cases III.a and III.b, respectively. Their locations are shown in Figures 4(d) and 4(e). As mentioned by the authors of these experiments, that study represents one of the few studies that measured the velocity field and wind pressure coefficient around buildings in the same experiment.

2.7. Metrics

Let's consider N sampling data points. Table 2 shows the metrics employed to quantify the agreement between the predicted and measured results, where O_i and P_i are the measured (reference) and predicted (computed) values for the sample i, respectively.

Table 2: Metrics to quantify the agreement between the predicted P_i and observed O_i results. The square brackets denote the averaging of the entire dataset.

Metric	Expression	Perfect agreement
RMSE	$\sqrt{\frac{1}{N}\sum_{i=1}^{N}(P_i - O_i)^2}$	0.0
NRMSE	$\dfrac{\text{RMSE}}{\sqrt{\frac{1}{N}\sum_{i=1}^{N}(O_i - [O])^2}}$	0.0
R^2	$1 - \dfrac{\sum_{i=1}^{N}(O_i - P_i)^2}{\sum_{i=1}^{N}(O_i - [O])^2} = 1 - \text{NRMSE}^2$	1.0
FB	$\dfrac{[O] - [P]}{0.5([O] + [P])}$	0.0
FAC2	$\frac{1}{N}\sum_{i=1}^{N} l_i \quad \text{with} \quad l_i = \begin{cases} 1 & \text{for } 0.5 \leq \dfrac{P_i}{O_i} \leq 2 \\ 0 & \text{else,} \end{cases}$	1.0
r	$\dfrac{\sum_{i=1}^{N}(P_i - [P])(O_i - [O])}{\sqrt{\sum_{i=1}^{N}(P_i - [P])^2}\sqrt{\sum_{i=1}^{N}(O_i - [O])^2}}$	1.0

The *residual* methods, i.e. those which evaluate the difference between observed and predict data, are

the most prevalent. The root mean square error (RMSE) prevents the negative-positive errors cancellation, it is expressed in the same units as the original data, and it leads to smooth functions of the residuals, a requirement for many optimization methods. Normalizing the RMSE is useful to compare predictions for variables of different natures. In particular, the standard deviation-based normalization of the RMSE (NRMSE) represents the ratio between the variation not explained by the predictive model and the overall variation in observed data. Similarly, the coefficient of determination (R^2) is the ratio of the explained variation to the total variation. The fractional bias (FB) indicates systematic prediction errors which lead to underestimating or overestimating the observed values. The fraction of the predictions within a factor of two of the observations (FAC2) is a robust metric as is not influenced by high and low outliers and highlighting deviations when the observed value is near zero. The Pearson correlation coefficient (r) reflects the linear relationship between two variables but it is insensitive to either an additive or a multiplicative factor. A perfect agreement is reflected by the metrics when R^2, FAC2 and r are 1, and RMSE, NRMSE and FB are 0. Finally, given a reference measured data set, the percentage of improvement of a predictive model j regarding another model k is quantified as

$$\text{Improvement} = \frac{\text{NRMSE}|_k - \text{NRMSE}|_j}{\text{NRMSE}|_k} \times 100\% \tag{19}$$

where the subindex denotes the prediction set used to compute the NRMSE.

3. Results

This section aims to present the closure coefficients obtained by optimization and the performance of the recalibrated turbulence model on the training and validation cases. In the following, we refer as Standard and Optimized for the k-ω SST models using the standard and optimized sets of closure coefficients, respectively.

3.1. The optimal set of closure coefficients

To carry out the optimization process, it is mandatory to build a reliable computational mesh for CFD simulations. Although an exhaustive study of the automatic mesher under similar conditions was previously carried out [52], a sensitivity analysis to mesh refinement is performed for the training case using Standard. Four hex-dominant volumetric meshes with approximately 300 K, 590 K, 1 M, and 2.8 M polyhedral cells were generated as coarse, intermediate, fine, and finest mesh configurations. Figure 5(a) presents snapshots of the meshes used. The refinement setting is equivalent for each mesh, but the cell sizes are scaled according to the reference cell size, DX. The table in Figure 5(b) shows the main characteristics of each mesh. The reference, maximum, and minimum cell sizes, DX, h_{max} and h_{min}, respectively, are reported with normalized values regarding the building height.

Using the C_p on sampling points with the finest mesh as the reference solution, the successive refinements yielded R^2 values of 0.9953, 0.9976, and 0.9987. for the coarse, medium, and fine solutions,

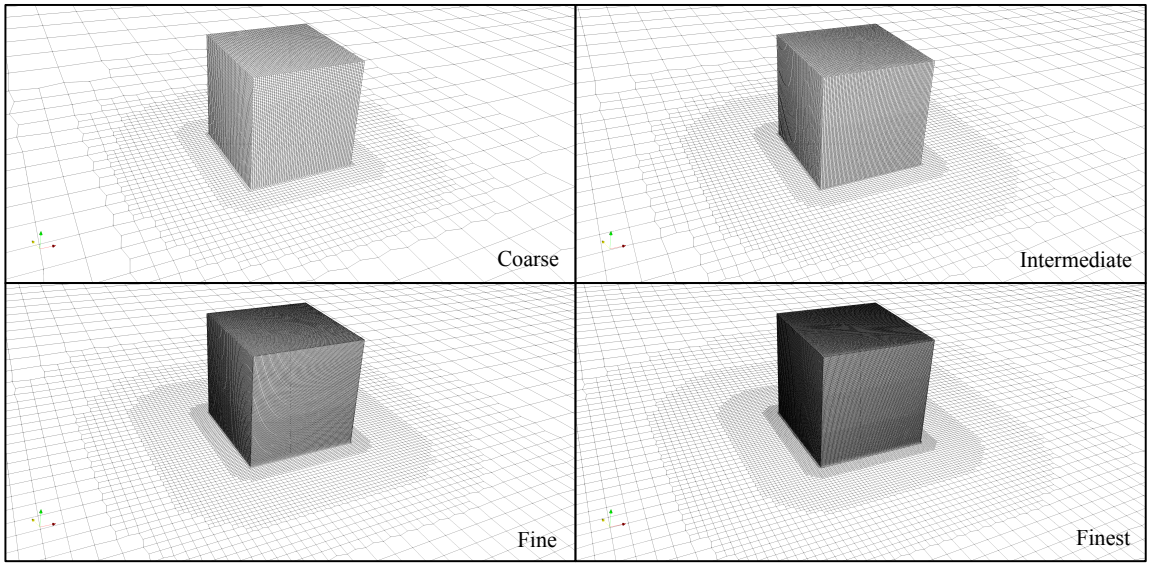

(a)

	# cells	DX/H	h_{max}/H	h_{min}/H	R^2 vs Finest
Coarse	300 K	1.20	6.00E-01	4.69E-03	0.9953
Intermediate	590 K	0.95	4.75E-01	3.71E-03	0.9976
Fine	1.0 M	0.70	3.50E-01	2.73E-03	0.9987
Finest	2.8 M	0.45	2.25E-01	1.76E-03	1.0000

(b)

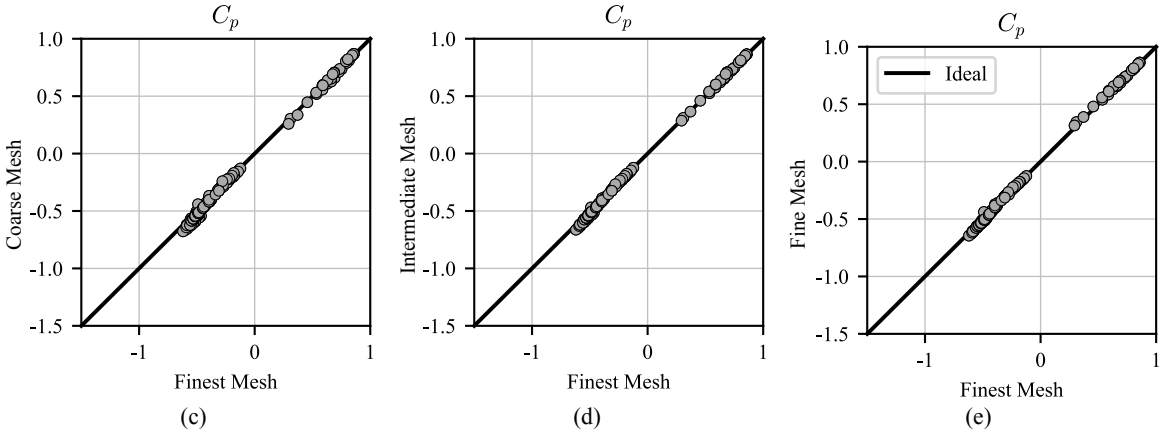

Figure 5: Sensitivity analysis to mesh refinement. Training case solved with the standard k-ω SST model. (a) snapshots of the meshes used, (b) summary of mesh configurations and fit, (c), (d), and (e) scatter of pressure coefficients computed with different mesh settings. The results with Finest mesh are taken as the reference.

as shown in Figure 5. These results, which reflect the consistency of the model, indicate that 99.5% of the variations, i.e. the spread, of the C_p values are determined, i.e. explained, by the location of the measurement point. In other words, less than 0.5% of the variation could be attributed to the mesh refinement. We consider this uncertainty low enough for any case, so the intermediate mesh configuration is selected to not outweigh the computational cost of the optimization procedure. Finally, the reference root-mean-square error, RMSE($\mathbf{x}^0$), is computed by comparing Standard predictions and experimental

	β^*	α_{k1}	α_{k2}	$\alpha_{\omega 1}$	$\alpha_{\omega 2}$	β_1	β_2	a_1	b_1	c_2	γ_1	γ_2
standard	0.090	0.850	1.000	0.500	0.856	0.075	0.083	0.310	1.000	10.000	0.555	0.440
optimized	0.997	3.746	0.782	2.951	4.945	0.848	1.121	1.070	1.124	1.507	0.377	0.331

(a)

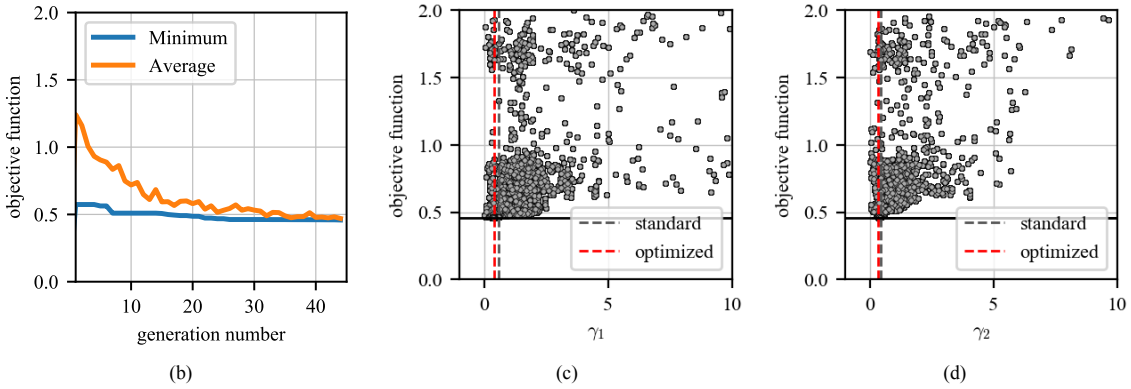

(b) (c) (d)

Figure 6: Insight into the optimization procedure. (a) the standard and the optimal sets of closure coefficients for the k-ω SST model. (b) evolution of the global objective function along the generations. (c) and (d) scatter of the aptitude of each individual regarding the γ_1 and γ_2 constants respectively, where dashed lines are their standard and optimized values.

data at sampling points, yielding a value of 0.305.

Once selected the computational mesh, the GA optimization with 80 initial individuals evolved through 45 generations is performed. The computational effort was dominated by the 7200 CFD simulations run, which took 150 hours on 80 cores, slightly more than 3 hours per generation. It is also worth noting that each CFD simulation performed preserves the HHABL condition throughout the fetch. The difference between the inlet (imposed) and the incident wind profile (evaluated 2H upstream of the building) is negligible. The optimized set of closure coefficients obtained is presented in Figure 6(a), where the standard coefficients are re-displayed to facilitate comparison. A general insight into the convergence of the procedure is presented in Figure 6(b). The evolution of the global objective function f for the best individual and the mean of f for all the individuals of the population from generation to generation is shown. It can be seen that f was reduced (i.e., the performance was improved) to 0.5, near the final minimum, after a few generations. After that, the convergence was slower until attaining the best value $f(\mathbf{x}^{\text{opt}}) = 0.458$ at the 45th generation. This individual leads a converged simulation ($\mathcal{R}$=0) with RMSE($\mathbf{x}^{\text{opt}}$)=0.139. The sufficiency of the number of generations is guaranteed because of the negligible difference between the average and minimum f at the end of the procedure. Figures 6(c) and 6(d) show the relationship between the constants γ_1 and γ_2 computed for each individual of each generation with the Equation (12) and the objective function. On the one hand, the effect of penalizing individuals who do not satisfy $\gamma_i > 0$ is observed. This penalty guarantees not to alter the physical meaning of these constants, which intervene as a multiplicative factor in the production term of ω, see Equation (5). On the other hand, despite being a non-linear combination of the other constants and that these assume values other than the standard ones, the value of each γ_i ends up near the standard value.

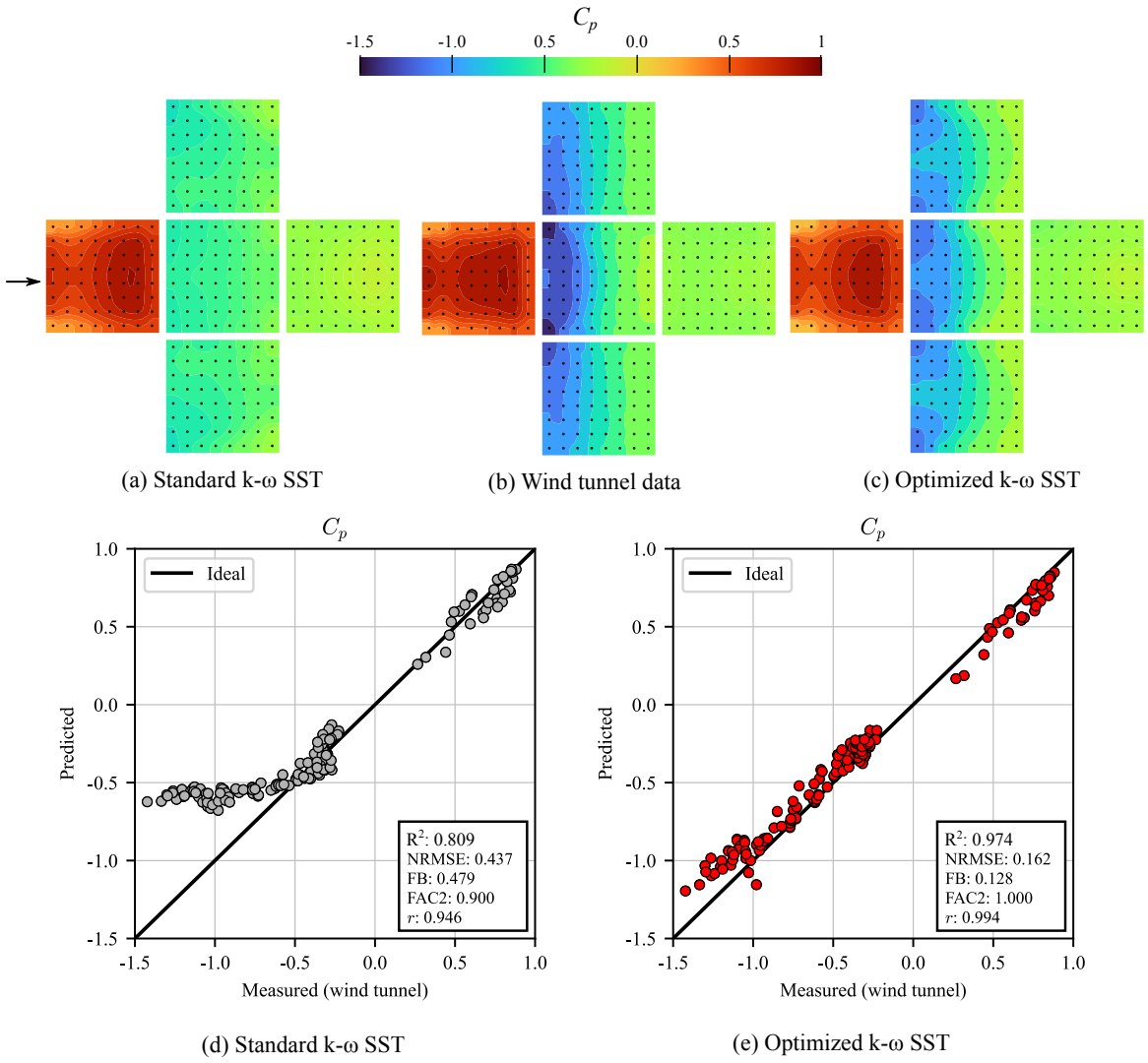

Figure 7: Comparison of wind tunnel data with Standard and Optimized results on the training case study. Wind pressure coefficients contours on building surfaces (a-c), fit of the numerical predictions against experimental data (d-e).

3.2. Performance of the optimized model

This section aims to explain the rationale behind Optimized outperforming the accuracy of Standard. Figures 7(a-c) display the pressure coefficients on each surface for the Standard and Optimized results and the reference data from the wind tunnel. A first observation is that the higher accuracy of Optimized compared to Standard is due to a better prediction of the negative pressures on the side surfaces and the roof of the building. The distribution of pressures measured in the experiment presents minima towards the corners of the leading edge of the roof. This feature is not perceptible in the results with Standard, which also overpredicts the pressure in that region. For its part, Optimized substantially improves the prediction of C_p in these regions. It captures the depression towards the corners of the building and the pressure recovery towards the leeward region.

Figures 7(d-e) present the fit at each measurement point via a scatter diagram. The metrics shown

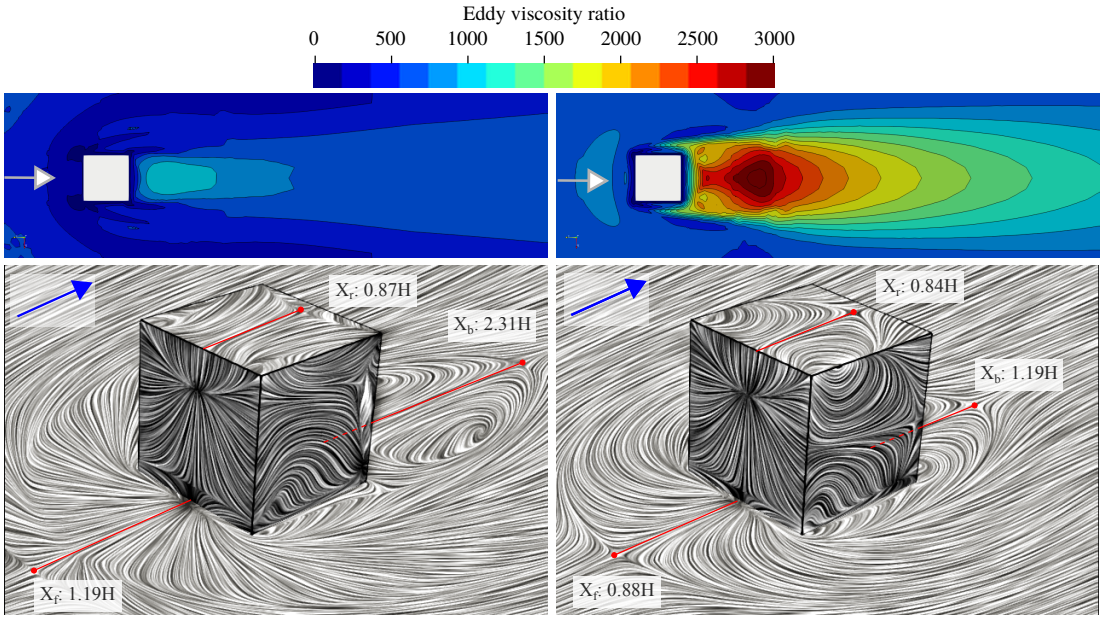

(a) Standard k-ω SST (b) Optimized k-ω SST

Figure 8: Training Case. Top: Eddy viscosity ratio fields on slice at 5H/12. Bottom: Shear velocity and reattachment lengths in front X_f, roof X_r, and back X_b. Wind tunnel reference are X_r=0.7H and X_b=1.2H [58].

quantify the fit by comparing the solutions to the Standard and Optimized models and experimental data. A significant gain in prediction is observed primarily for $C_p < -0.5$ samples. The overall improvement computed with Equation (19) is 63%. Each metric evaluated leads to similar conclusions. It is noteworthy that the FAC2 takes the optimal value in the calibrated case. At the same time, a slight deterioration in the prediction of positive pressures on the windward surface can be observed.

Although the objective is to adjust the pressure coefficients on the building, this calibration impacts the prediction of the flow around the building. In Figure 8, the computed shear velocity on the surfaces of the cube and the ground is presented via the line integral convolution (LIC) representation technique. In turn, the reattachment lengths in front (X_f), on the roof (X_r,) and behind the building (X_b) are presented.

The observed flow patterns, see Figure 8, show that both the flow over the roof and around the sides detach at the windward edge but do reattach. The streamlines near the ground upstream of the cube show reversed flow, while the separation bubble behind the building is reflected through two symmetric vortex patterns on the floor and finally reattaches at X_b from the rear surface.

The Reynolds number, $\mathrm{Re_H} = 8.8 \times 10^4$, is calculated using the building's height, H, and the velocity at this height. Among the diverse literature available with experimental data on reattachment lengths for flows around a cube [59], the simulated conditions in our study are similar to those of Murakami [58]'s wind tunnel test. That work reports X_r=0.7 H and X_b=1.2 H. The results obtained with Optimized, X_r=0.84 H and X_b=1.19 H, fit the experimental data much better than the standard case (0.87H and 2.31

H, respectively), mainly for the reattachment length on the ground behind the building. It is important to note that the flow characteristic fit was not explicitly calibrated; however, the improvement in its prediction is an added benefit of the optimization. This fact confirms the proper selection of the objective function and the enhanced ability of the optimized model for the prediction of the flow around a bluff body.

The turbulent eddy viscosity to laminar kinematic viscosity ratio (ν_t/ν) is the eddy viscosity ratio. The top of Figure 8 shows the contour maps of the eddy viscosity ratio on a slice at height 5H/12 for the Standard and Optimized solutions. It can be seen that the recalibrated turbulence model increases momentum diffusion in the wake region by up to three times. A higher eddy viscosity means a higher turbulent transfer of energy as a result of moving eddies, which causes a stronger dissipation of flow inertia in these regions. These differences help to explain the optimized model's improved prediction of reattachment length and negative pressures.

3.3. Validation Case I

To assess the generalizability of the optimized model in non-isolated environments with different levels of clustering, simulations of the validation Case I were conducted using Standard and Optimized.

Computational meshes of Cases I.a, I.b, and I.c were generated considering a reference cell size DX equivalent to the one selected in the training case. Details of the meshes are shown in Figure 9 where the target (central) building is colored. The number of cells is 1.64 M, 1.58 M, and 2.39 M for Cases I.a, I.b, and I.c respectively, with more than 95% of hexahedra each. More features of the meshes are given in Figure 9(d).

Figure 10 reports the prediction accuracy of both models for the pressure coefficients at the measurement points on the target building's surfaces. Every metric evaluated shows a better agreement of Optimized with the reference data than Standard. The Improvement summarizes the enhancement obtained with Optimized for each case study, which is between 25 and 30%. It can be seen that, for both models, the fit decreases when the area density CA increases.

Figures 10(b-d) depict the scattered data for each case study that was solved using both models. It is observed that Optimized has a lower dispersion around the ideal fit. These graphs also demonstrate the C_p ranges' sensitivity to area density. The range (-1.5 to 0.8) for CA=0.1, is narrowed up to (-0.65,0.2) for CA=0.4. The standard model is not able to accurately predict the proper range of pressures, particularly in the skimming flow case. Lower predictability (R^2=0.309) is mainly due to obtaining an excessively homogeneous pressure field around the target building. These deficiencies are ameliorated by Optimized. The level of predictability of the models also varies with the wind incidence angle, as can be seen in the table in Figure 10(a). The results keep the advantages of the optimized model in terms of accuracy. The standard model fails more on the computation of pressure coefficients for wind angles with a perpendicular approach to the building (0° and 90°) than for oblique angles. In fact, for Case I.c and 0°, Standard is not predictive at all, as the R^2 is negative. A graphical analysis of the results varying

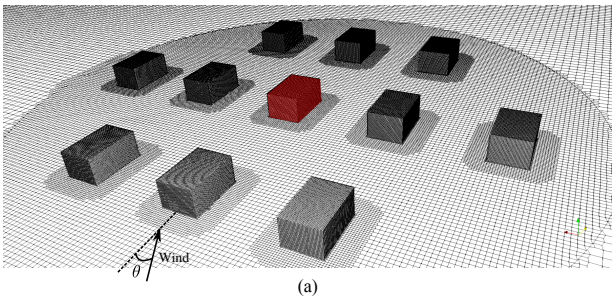

(a)

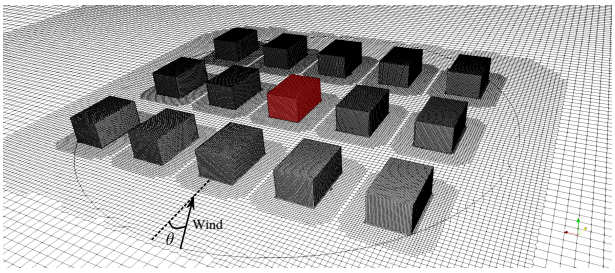

(b)

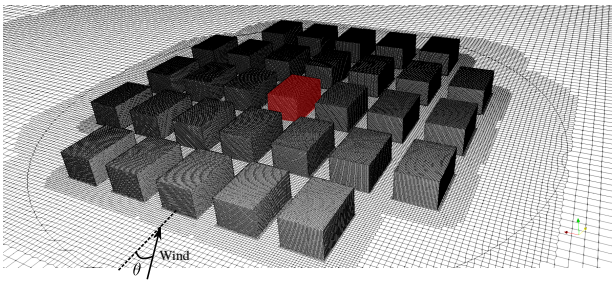

(c)

Case	#cells	Domain (m)		cell size (m)		Skew	Non-ortho	y^+
		Width	Height	Max	Min	Max	Max	Avg
I.a	1.64 M	6.49	0.72	0.11	0.0011	2.33	68.4	2.51
I.b	1.58 M	4.73	0.72	0.11	0.0012	2.33	68.4	2.38
I.c	2.39 M	5.22	0.72	0.11	0.0013	1.70	57.9	1.88

(d)

Figure 9: Validation Case I. Urban area of the computational meshes for Cases I.a, I.b, and I.c (a-c). Their characteristics as the number of cells, dimensions of the cylindrical computational domain, maximum (Max) and minimum (Min) cell sizes, skewness (Skew), non-orthogonality (Non-ortho) and averaged y^+ on building surfaces are summarized in (d).

the wind incidence angle is found in Figure 11. There, the Standard and Optimized predictions of the surface-averaged pressure coefficient on selected surfaces for each case study and wind incidence angle are presented and compared with the wind tunnel measurements. In the case of the windward surface, the predictions with the Optimized are closer to the experimental reference. In each case study, Standard underpredicts the pressure on Surf-1, which is related to the overestimation of the reattachment length observed in the isolated building. For any wind incidence angle, the target is behind a neighbor building, therefore the ability of the optimized model to estimate shorter reattachment lengths allows for predicting a higher pressure recovery, improving the accuracy of the results.

Figure 12 displays the pressure coefficients on the surfaces of the target building for a wind incidence angle of 22.5°. As the urban density increases, the pressure field is more homogeneous. This leads to

Case	k-ω SST	R^2 for wind incidence angle					Total					
		0º	22.5º	45º	67.5º	90º	R^2	FB	FAC2	r	NRMSE	Improvement [%]
I.a	Standard	0.528	0.804	0.696	0.841	0.714	0.729	0.285	0.786	0.886	0.520	-
	Optimized	0.806	0.926	0.861	0.938	0.652	**0.857**	**0.280**	**0.868**	**0.960**	**0.378**	**27.3%**
I.b	Standard	0.202	0.728	0.741	0.399	0.181	0.551	0.325	0.619	0.808	0.670	-
	Optimized	0.767	0.818	0.803	0.607	0.478	**0.748**	**0.330**	**0.834**	**0.930**	**0.502**	**25.1%**
I.c	Standard	-0.218	0.296	0.590	0.239	0.470	0.323	-0.015	0.881	0.570	0.823	-
	Optimized	0.568	0.704	0.677	0.693	0.598	**0.667**	**-0.004**	**0.906**	**0.884**	**0.577**	**29.9%**

(a)

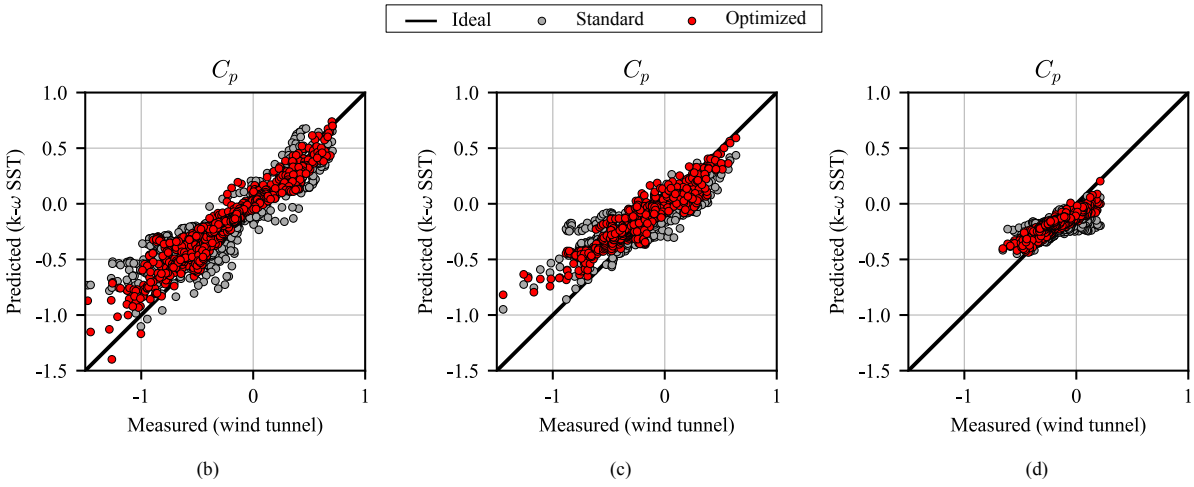

(b) (c) (d)

Figure 10: Validation Case I. Statistics of the pressure coefficients prediction with Standard and Optimized (a). Scattered data of each measurement point for both models in Cases I.a, I.b, and I.c respectively (b-d).

smaller pressure differences between windward and leeward surfaces. The pressures on the roof and the cavity region, i.e. the surfaces in the wake, are well captured by the optimized model. The prediction of positive pressures on windward surface agrees well with the wind tunnel data, with larger discrepancies in Case I.c. On the other hand, the location of the minimum pressure is accurately placed by the Optimized on the roof, but its absolute value (-1.7, -1.4, and -0.7) is slightly underpredicted (-1.5, -0.9, and -0.4) for the three case studies. In this regard, the situation with Standard is worsen as the minimum pressures are (-1.2, -0.9, and -0.3) respectively.

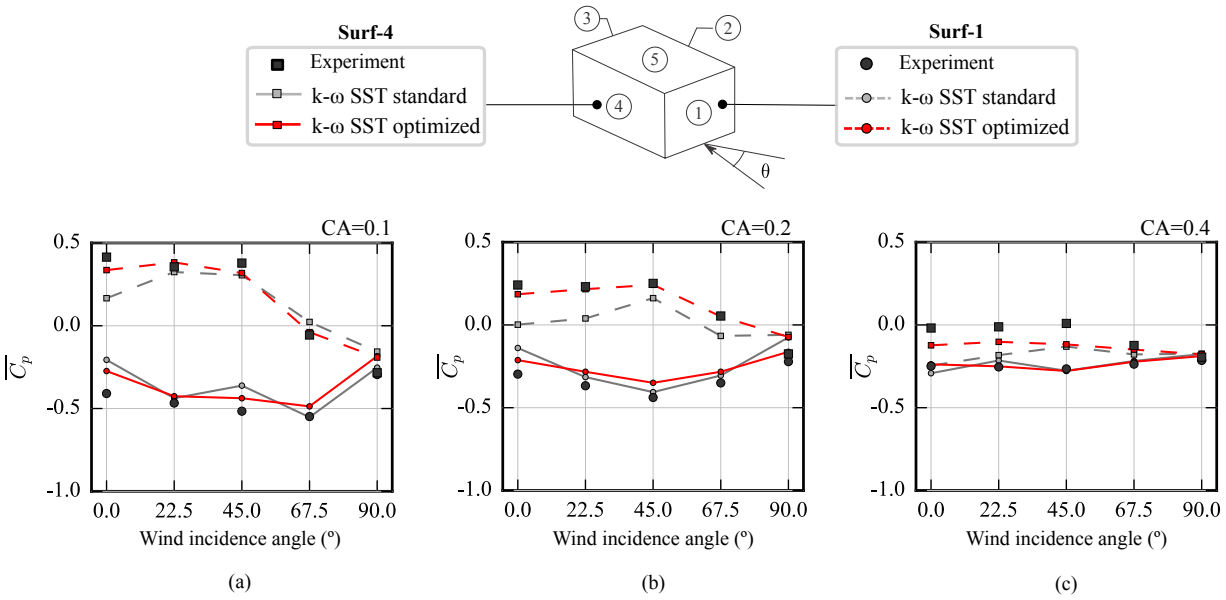

Figure 11: Validation Case I. Surface-averaged pressure coefficients on target building's surfaces 1 and 4 for different wind incidence angles. Comparison between wind tunnel measurements and predictions with Standard and Optimized. Cases (a) I.a, (b) I.b and (c) I.c.

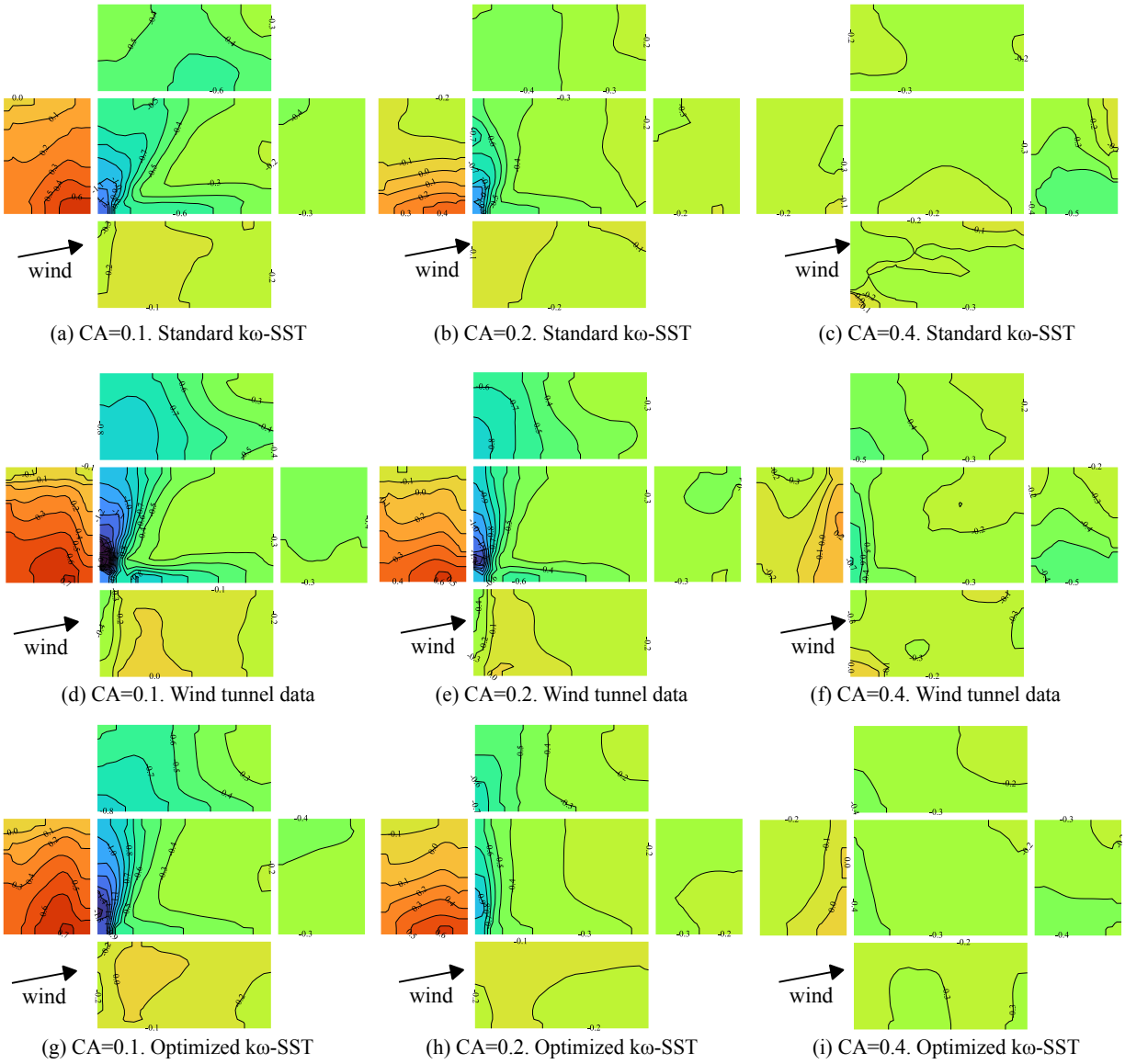

(a) CA=0.1. Standard kω-SST (b) CA=0.2. Standard kω-SST (c) CA=0.4. Standard kω-SST

(d) CA=0.1. Wind tunnel data (e) CA=0.2. Wind tunnel data (f) CA=0.4. Wind tunnel data

(g) CA=0.1. Optimized kω-SST (h) CA=0.2. Optimized kω-SST (i) CA=0.4. Optimized kω-SST

Figure 12: Validation Case I. Contours of surface pressure coefficients on target building for a wind incidence angle 22.5º. Experimental data are shown in the center, subfigures (d), (e) and (f). Predictions with Standard are shown above (a), (b) and (c), and with Optimized are displayed below in (g), (h) and (i).

3.4. Validation Case II

Computational meshes were generated considering reference cell size DX=H similar to the one selected in the training case. The number of cells is 2.07 M, 2.22 M, and 1.54 M for Cases II.a, II.b, and II.c respectively, with more than 96% of hexahedra each. Details of the meshes are presented in Figure 13. It should be noted that the mesher used incorporates prismatic layers both on the buildings and on the ground of the urban scene. This last characteristic is necessary for the studies of the flow at the pedestrian level that are carried out in this subsection. In particular, the meshes obtained have on the ground an average y^+ of 1.5 and a maximum of 50, being reasonable for the use of an automatic near-wall treatment approach.

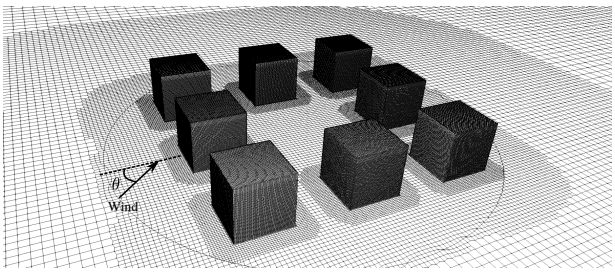

(a)

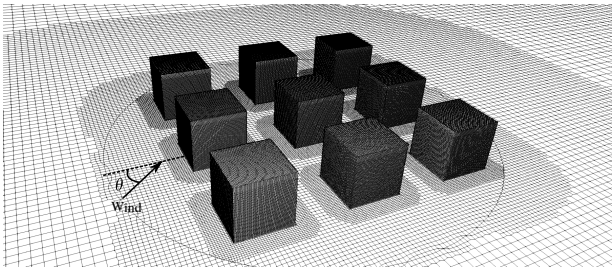

(b)

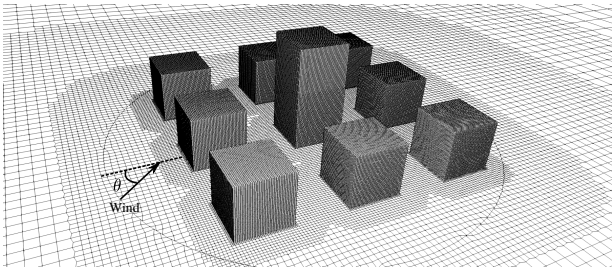

(c)

Case	#cells	Domain (m)		cell size (m)		Skew	Non-ortho	y^+
		Width	Height	Max	Min	Max	Max	Avg
II.a	2.07 M	3.47	1.20	0.08	0.0009	3.36	77.8	0.77
II.b	2.21 M	3.47	1.20	0.08	0.0009	2.77	77.8	0.75
II.c	1.54 M	6.40	2.40	0.18	0.0015	1.67	57.5	0.94

(d)

Figure 13: Validation Case II. Urban area of the computational meshes for Cases II.a, II.b, and II.c (a-c). Their characteristics as the number of cells, dimensions of the cylindrical computational domain, maximum (Max) and minimum (Min) cell sizes, skewness (Skew), non-orthogonality (Non-ortho) and averaged y^+ on building surfaces are summarized in (d).

Case	k-ω SST	R^2 for wind incidence angle			Total					
		0º	22.5º	45º	R^2	FB	FAC2	r	NRMSE	Improvement [%]
II.a	Standard	-1.278	0.066	-0.423	-0.445	**-0.061**	**0.853**	0.662	1.202	-
	Optimized	-0.878	0.414	0.573	**0.147**	0.212	0.819	**0.835**	**0.924**	**23.1%**
II.b	Standard	-1.444	-0.941	-0.232	-0.637	-0.147	**0.903**	0.747	1.279	-
	Optimized	0.041	0.268	0.387	**0.315**	**0.121**	0.892	**0.866**	**0.827**	**35.3%**
II.c	Standard	-0.573	0.242	0.341	0.223	**0.085**	0.872	0.834	0.882	-
	Optimized	-0.369	0.387	0.494	**0.364**	0.209	**0.911**	**0.911**	**0.798**	**9.5%**

(a)

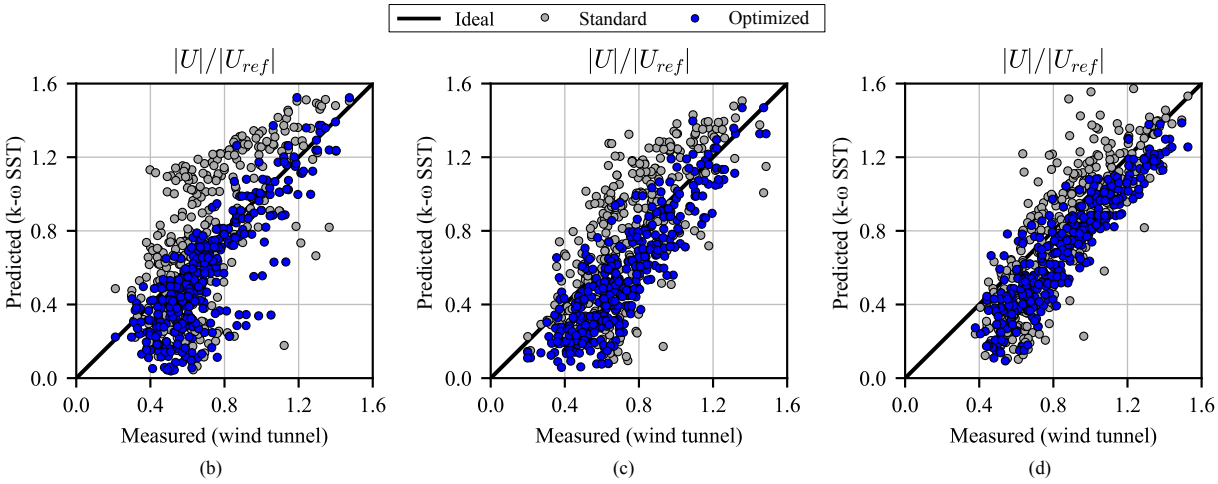

Figure 14: Validation Case II. Statistics of the prediction of velocity magnitude with Standard and Optimized (a). Scattered data of each measurement point for both models in Cases II.a (no central building), II.b (central building with 1H), and II.c (central building with 2H) respectively (b-d).

To set the basis for the comparison, the velocity results that are obtained from the simulations at the measurement points are normalized by the inlet velocity at the measurement height of 0.1H, $|U_{ref}|$.

The results for the three analyzed wind directions and the three case studies are presented in Figure 14. Figure 14(a) presents the quantitative analysis of the prediction errors with the Standard and Optimized regarding the velocity magnitude measured experimentally. Figures 14(b-d) displays the scattered data between the AIJ experiment (x-axis) and simulations (y-axis) for the cases considering no central building (Case II.a), a central building with the same (Case II.b) or twice (Case II.c) the height of its neighbors.

As in the previous case, the optimization improves the prediction of the standard model in each scenario. The maximum enhancement is achieved in Case II.b, where the agreement with the experimental measurement is increased by 35.3%.

In any case, the predictions of flow at the pedestrian level with both k-ω SST models are reliable enough under the perspective of the FAC2 metric, where the worst value of 0.819 is get. However, the deviations measured in terms of the NRMSE are greater than those found in computing pressure coefficients. From the results, a pronounced underprediction of the velocities can be observed. The largest mismatches can be identified with the measurement points located in the canyons between buildings, mainly in Case II.a when the central building is absent.

Standard obtains a negative total determination coefficient for Cases II.a and II.b, which is reflected

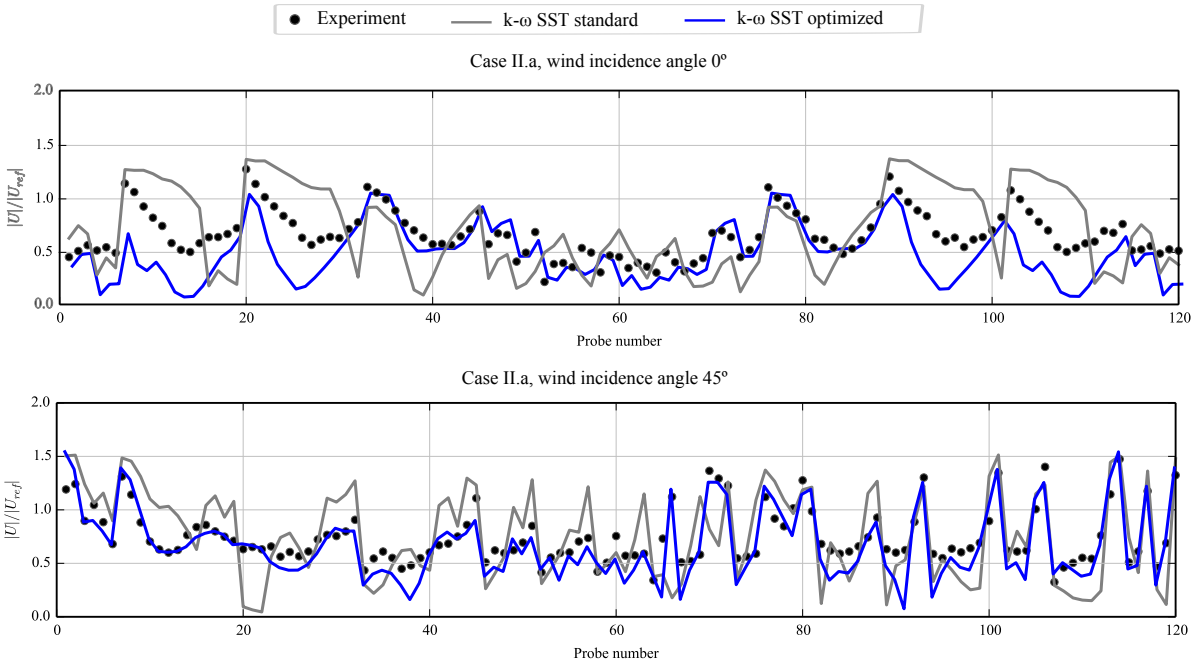

Figure 15: Validation Case II.a. Velocity measurements ordered by label number. Comparison between the experimental data set and predictions with Standard and Optimized for 0° and 45° wind and central building height 0H.

by a poor correlation coefficient and highlights the excessive dispersion of the predictions. Optimized substantially improves the correlations with the experimental data but highlights the underprediction of the velocities, which hurts the bias factors.

From the results, it can be observed that the presence, or not, of the central building and the variation of its height affects the predictability of the evaluated models to a lesser extent. The opposite is observed when analyzing the sensitivity to the wind angle of incidence. Although Optimized improves the Standard predictions, significant deviations are still observed when the flow is aligned with the canyons between buildings (0°).

Figure 15 presents comparisons between the wind tunnel measurements and CFD predictions for the velocity magnitude. The data is ordered following probe numbers, see the labeling in Figure 4(c). Two wind incidence angles, 0° and 45°, of the scenario without a central building (Case II.a) were selected. When the wind is aligned with the buildings, the experimental measurement describes an acceleration associated with the wind entering between the three upwind buildings. The velocity slows down when reaches the cavity region behind them, see sequences 20-32 and 89-101 for example. While Standard overpredicts velocities in these regions, Optimized mainly underpredicts them in sensor sequences 7-19 and 102-114. The optimized model substantially improves the fit in the wake regions, see probes 46-75, favored by a good prediction of the velocities in sequences 33-45 and 76-88. When the wind is oblique to the urban center, no noticeable flow channeling is found. This increases the reliability of the Optimized, as observed in the comparison of the case at 45° which is quantified with $R^2 = 0.573$. Standard is still

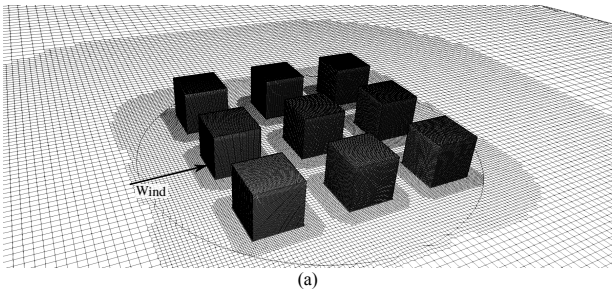

(a)

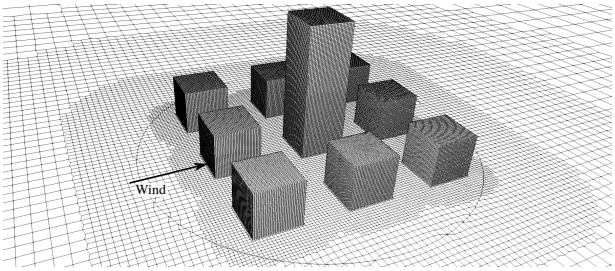

(b)

Case	#cells	Domain (m)		cell size (m)		Skew	Non-ortho	y^+
		Radius	Height	Max	Min	Max	Max	Avg
III.a	2.22 M	1.73	0.60	0.04	0.0005	3.01	77.9	0.24
III.b	1.04 M	4.71	1.80	0.12	0.0009	1.48	57.4	0.49

(c)

Figure 16: Validation Case III. Urban area of the computational meshes for Cases III.a, and III.b (a-b). Their characteristics as the number of cells, dimensions of the cylindrical computational domain, maximum (Max) and minimum (Min) cell sizes, skewness (Skew), non-orthogonality (Non-ortho) and averaged y^+ on building surfaces are summarized in (d).

erratic, with sparse predictions obtaining a negative coefficient of determination of $R^2 = -0.423$. The above also applies to the scenarios with the central building (Cases II.b and II.c), where the improvement achieved by Optimized can be explained under a similar analysis, but is not shown for conciseness.

3.5. Validation Case III

Computational meshes were generated considering a similar setting to the one used previously. Cases II.b and III.a have geometries that differ by a scale factor of 2. The automatic mesher then leads to a mesh of 2.22 M cells for Case III.a. For Case III.b the target building height is 3 H, then the computational domain is increased to preserve the blockage ratio. Consequently, the reference cell size DX is redefined, which leads to a discretization of 1.04 M cells. Snapshots and details of the characteristics of the meshes are presented in Figure 16. The measurements are normalized to set the basis for the comparison. For that, velocity, pressure, and turbulent kinetic energy at the sampling points are normalized using the inlet velocity at the height H, $|U_H|$.

Figure 17 compares the velocity magnitude predictions over a vertical plane at y/H = 0 for the different sets of coefficients when the central building has a height of 1 H (Case III.a). The quantitative analysis in the table of Figure 17(a) reports that Optimized led to a substantial improvement regarding Standard, i.e. over 40%. Figures 17(b-c) shows the velocity field in the upwind and downwind cavities. The

Case	k-ω SST	$\|U\|/\|U_H\|$ predictions					
		R^2	FB	FAC2	r	NRMSE	Improvement [%]
III.a	Standard	0.797	0.168	0.800	0.913	0.450	-
	Optimized	**0.927**	**0.125**	**0.944**	**0.978**	**0.269**	**40.2%**

(a)

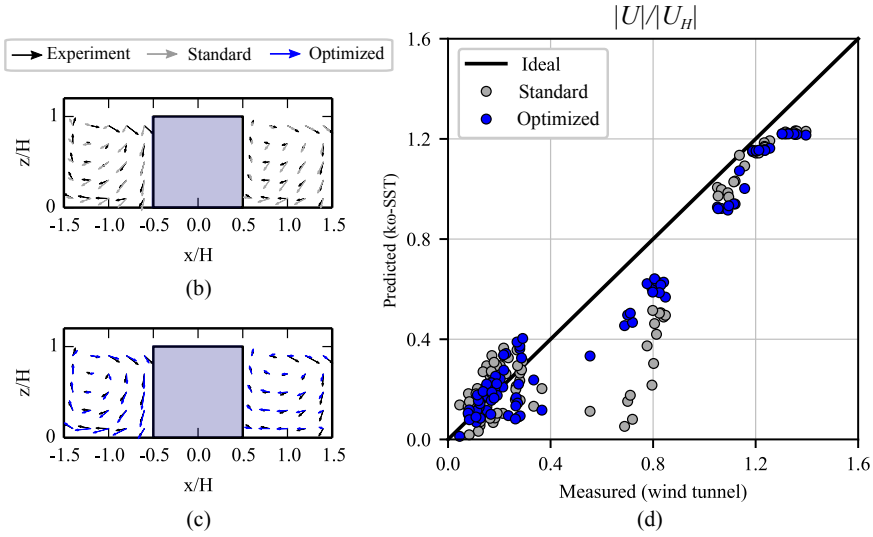

Figure 17: Validation Case III.a. Statistics of the prediction of velocity magnitude with Standard and Optimized (a). Comparison of measured and predicted wind field around the target building (b-c). Scattered data of each measurement point (d).

experimental measurement showed circulations near both façades of the target building. The downwind circulation is reproduced by both models, but Standard fails to predict its location and intensity, which is more accurately estimated by Optimized. This improvement achieved with Optimized is accentuated when recirculation in the upwind cavity is analyzed, as this feature of the flow is not even reproduced by Standard.

Figure 18 compares the velocity magnitude predictions over a vertical plane at y/H = 0 for Standard and Optimized models when the central building has a height of 3 H (Case III.b). Figure 18(a) summarizes the calculation results of the metrics using all measurement points over the vertical plane. Although in this case study the fit obtained by Standard is reliable, the improvement achieved by Optimized is greater than 40%. A comparison of the velocity in the upwind and downwind cavities is shown in Figures 18(b) and 18(d). The strong reverse flow observed in the experimental results in the downwind cavity behind the high-rise building is accurately reproduced by both models. Again, the largest differences can be found in the upwind cavity, where Optimized corrects the underestimation of velocities by Standard.

Figures 19(b) and 19(d) compare the distributions of the wind pressure coefficient over the centerline of the windward façade, roof, and leeward façade in Cases III.a and III.b respectively. On the windward surface, experimental measurements of C_p in Case III.a are close to zero and the pressure difference between the windward and leeward walls is slightly positive. This tendency is well predicted by Optimized, but Standard fails due to underpredict the pressure in the upwind cavity. In Case III.b, large positive values of

Case	k-ω SST	$\|U\|/\|U_H\|$ predictions					
		R^2	FB	FAC2	r	NRMSE	Improvement [%]
III.b	Standard	0.746	**0.015**	0.874	0.864	0.504	-
	Optimized	**0.912**	0.064	**0.947**	**0.962**	**0.296**	**41.3%**

(a)

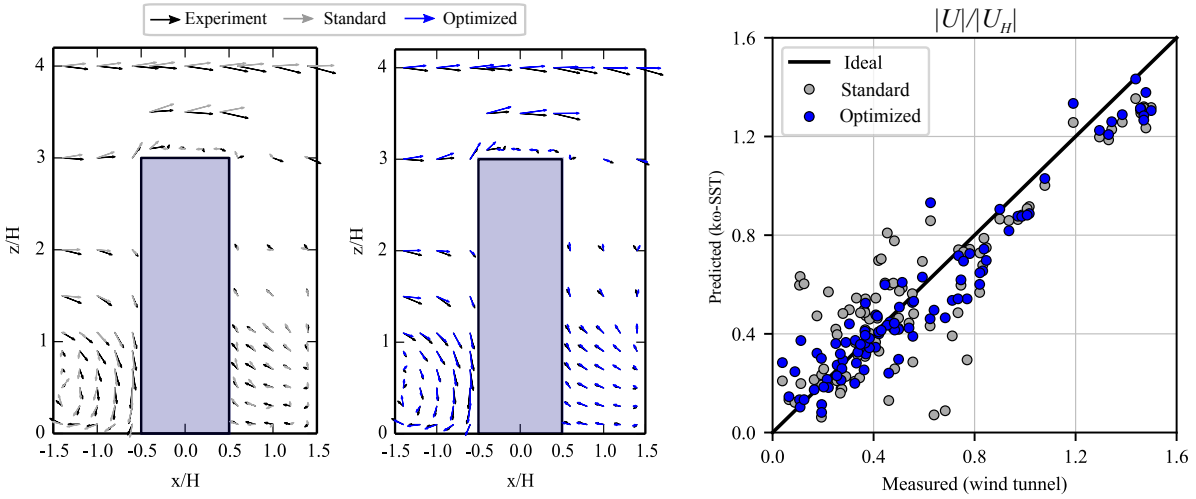

(b) (c) (d)

Figure 18: Validation Case III.b. Statistics of the prediction of velocity magnitude with Standard and Optimized (a). Comparison of measured and predicted wind field around the target building (b-c). Scattered data of each measurement point (d).

C_p were measured on the windward façade. Larger negative values than in Case III.a are observed in the downwind cavity due to the suction effect of the upwind flow in the wake region. The high-rise building enlarges the pressure difference between the windward and leeward surfaces below the height of the surrounding buildings. In this regard, Optimized is accurate about this behavior while Standard largely overpredicts that C_p difference. For C_p values on the roof, a uniform distribution was experimentally obtained in Case III.a. The negative values at approximately C_p=-0.1 are well predicted by both models. However, in Case III.b, C_p measured was very low due to the stronger separation at the roof corner, i.e., approximately C_p=-1.0 over half the length of the roof. As expected, Standard underpredicts the pressure, while a slightly excessive correction is done by Optimized. As the pressure coefficients are close to zero in Case III.a, any deviation has a noticeable impact on the fit metrics evaluated. For this reason, Optimized improves the Standard predictions by approximately 76%. Likewise, in Case III.b the improvements obtained with Optimized reach 23%. In both cases, the improvement in accuracy is dominated by fusing a better prediction of the pressure differences between the windward and leeward façades.

Figures 19(c) and 19(e) shows the distribution of TKE over the vertical plane for cases III.a and III.b respectively. Noticeable differences between the TKE numerical results using Standard and Optimized with the experimental measurements are observed in both scenarios. The values are largely underestimated by both methods behind the target building. These are better predicted in the upwind cavity by both

Case	k-ω SST	C_p predictions		k/U_H^2 predictions	
		NRMSE	Improvement [%]	NRMSE	Improvement [%]
III.a	Standard	2.660	-	1.635	-
	Optimized	**0.644**	**75.8%**	**1.333**	**18.5%**
III.b	Standard	0.271	-	1.360	-
	Optimized	**0.208**	**23.2%**	**1.092**	**19.7%**

(a)

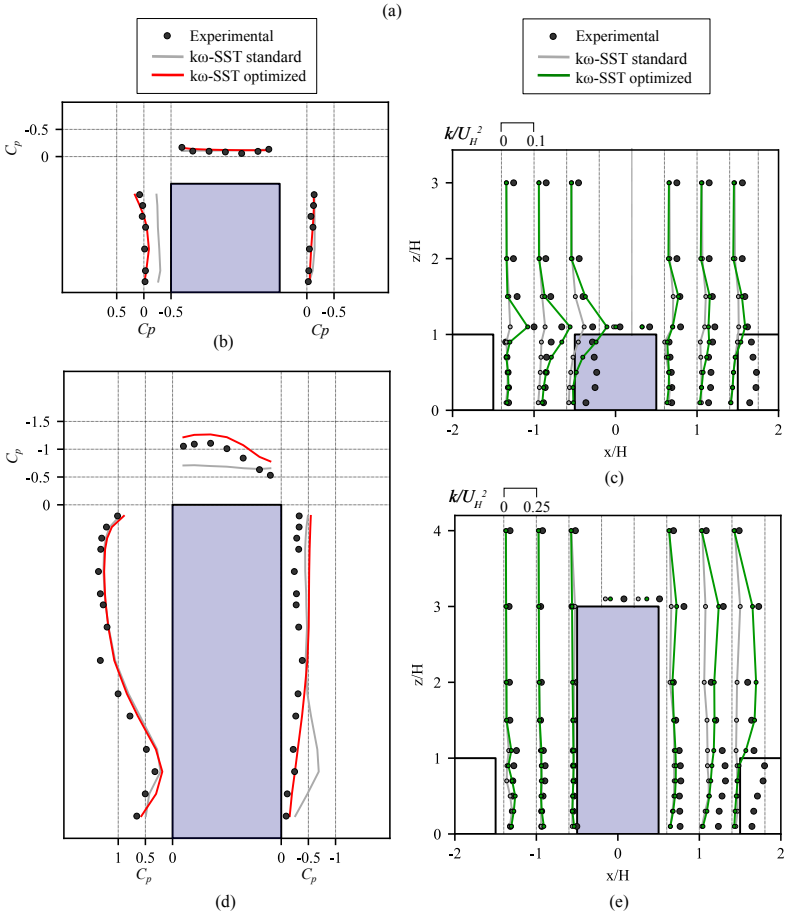

Figure 19: Validation Case III. Statistics of the prediction of pressure coefficients and normalized kinetic energy with Standard and Optimized (a). Comparison of measured and predicted C_p and k/U_{H^2} fields around the target building in Case III.a (b-c). Comparison of measured and predicted C_p and k/U_{H^2} fields around the target building in Case III.b (d-e).

models, worsening towards the windward façade in the low-rise building case. A slight enhancement of the prediction accuracy of almost 20% is obtained using Optimized.

4. Discussion

The current industrial practice of CFD simulation to predict urban airflows employs almost exclusively a RANS modeling approach. The time-averaged solutions give valuable data in a reasonable computing time, but the effectiveness of its application depends on the reliability of RANS solutions.

Structural and parametric uncertainties hamper the predictions based on RANS turbulence modeling. While the structural ones are related to the modeling hypothesis as the Boussinesq approximation, the parametric ones arise from the values of closure coefficients. Both are epistemic and could be alleviated by

leveraging additional knowledge of turbulent flow physics or by more abundant/accurate data becoming available. This work addressed the second alternative exploiting current state-of-the-art computational techniques, such as genetic algorithms and efficient CFD codes running in high-performance computing facilities. A data-driven procedure replaces the required expertise in turbulent flow physics for fine-tuning the closure coefficients. This approach solves the minimization problem in Equation (15). The product of this study is an optimized k-ω SST turbulence model that consistently outperforms the accuracy of the standard version to predict urban airflow. This validates the application of the set of optimized constants, in replace of standard ones, to enhance the reliability of the solutions of the wind flow around isolated and urban buildings.

The accuracy of the results reached in this research can be compared with similar studies in the literature. The prediction of the standard k-ω SST model presents an acceptable agreement with wind tunnel measured data. However, there is a noticeable tendency to overestimate the predicted velocities in high-speed areas and insufficient negative pressures in the wake regions. This trend is because of the underestimating momentum diffusion of RANS modeling, i.e., the mixing caused by large transient fluctuations caused by building geometries [16, 26, 60]. The deficiency described may explain the decreased performance of RANS models as area density increases in Case I. In the skimming flow regime, large-scale flow structures are not dominant and deviations in the turbulence prediction have more impact. Consequently, the accuracy is highly sensitive to the wind incidence angle under study. For instance, the agreement with reference data is lower for cases with normal wind incident angles (i.e., 0° and 90°); see Tables in Figures 9(a) and 14(a). The lowest accuracy for the prediction of the velocity field in the upstream and downstream cavities and underestimation of the momentum diffusion in these areas result in low differences of wind surface pressure coefficient over the windward and leeward façades against the normal wind angle. The deviations in pressure coefficients and velocity estimations are palliated when oblique wind incidence angles are analyzed. The occurrence of this phenomenon in the structured arrangement of buildings was also reported in Ref. [61], while in Ref. [62] a similar conclusion is reached when the same validation (Case II) is analyzed.

In this investigation, the results proved that it is possible to increase momentum diffusion and shorten the predicted wake length by tuning the closure coefficients of the turbulence model. Consequently, thereby improving prediction accuracy in urban scenarios. The optimized model consistently outperforms its standard version concerning the agreement with experimental data. Thus, the use of the new set of coefficients in the k-ω SST model yields higher accuracy in all validation cases and for almost all the metrics evaluated in this work. These findings allow us to strongly recommend to CFD practitioners the use of the recalibrated k-ω SST model in their daily tasks for urban applications. It is also worth noting that the optimized model inherits accuracy issues from its RANS formulation. The structural uncertainty related to the Boussinesq hypothesis was not addressed in this paper and limits the generality of the results since the real solution may lie outside the solution space of the formulation [7]. Moreover,

some discrepancies, such as the significant deviations in the predictions of TKE in cavities could only be corrected using more complex turbulence models [40, 63].

An impairment of the generality of the calibrated parameters could be related to the experimental data because the optimization procedure does not consider observational uncertainties. Although the careful selection of the most reliable databases, available sources are not free from measurement or processing errors and biased data. This inconsistency of measured data reported from different wind tunnels has been acknowledged as a long-standing issue by the wind engineering community [64]. Selecting training and validation data required a thorough analysis of the experimental data. This process found various inconsistencies. For example, in the training case (isolated cube, from TPU), the configurations at angles of incidence 0^{o} and 90^{o} should be equivalent under certain symmetry. However, the published pressure coefficients differ markedly. Moreover, the measurements in the case of 0° are not symmetric regarding the wind incidence axis, which demanded the data curing mentioned in the corresponding section. In addition, the available data from Case III (Ref. [56]) suffer from errors in the coordinates of the pressure sampling points, which were corrected before their use in the validation. This curing process was as exhaustive as possible but leaves room for an additional source of uncertainty. Lastly, TPU data provides slightly larger negative pressure coefficients than other databases [65]. These deviations in the selected training data are related, but not limited, to the different turbulent intensities of the inlet wind. This fact could explain the overprediction of negative C_p when validating the optimized model in Case III.b. Therefore, future work becomes challenging considering observational uncertainties in the optimization process as a strategy to get unbiased models.

5. Summary and conclusions

An enhanced k-ω SST model for the accurate prediction of urban wind flow has been developed. To do this, a non-linear optimization procedure that couples a genetic algorithm with computational fluid dynamics (CFD) simulations was implemented. To determine the set of optimal closure coefficients, the prediction error by CFD simulations regarding a set of wind tunnel measured pressure coefficients was minimized. To validate the predictions of the enhanced k-ω SST model for wind flows in urban environments, an exhaustive assessment was carried out over many case studies taken from three different wind tunnel experiments. This validation carefully examined the predictions of mean pressure coefficients on building surfaces, as well as the mean velocity and turbulent kinetic energy (TKE) fields in pedestrian wind environments. Several metrics were employed to quantify the agreement between CFD results and wind tunnel data.

In the training case, which comprises an isolated cubic building, the optimized model reduces the error of the wind pressure prediction by 63% compared to the standard model. This improvement is due to a more accurate estimation of the low pressures in the wake regions. Moreover, the enhanced turbulence model also improves the prediction of other relevant flow features, such as reattachment lengths, which

indicates that the new model better represents the whole flow physics. Regarding the validation results, the reliability of the RANS models decreased when area density increased or high-speed regions between buildings were studied. These facts are closely related to the significant deviations in the predictions of TKE from the wind tunnel measurements, mainly for incident wind angles aligned with urban canyons. Overall, the optimized k-ω SST model is consistently more accurate than the standard one, mainly because of the increased momentum diffusion in wake regions. Thus, this feature enables the calibrated model to estimate shorter reattachment lengths and predict a faster pressure recovery behind buildings. The normalized root mean square error for a point-by-point prediction is reduced by above 75% in pressure, 40% in velocity, and 20% in turbulent kinetic energy.

Despite the inherited limitations from the standard turbulence model in predicting flow behavior around bluff bodies and sheltered conditions, the optimized model achieves significant improvements in CFD accuracy to predict urban wind flows. Therefore, the proven capacity for adaptation via recalibration, as well as their low computational cost, reinvigorate RANS turbulence models as the most convenient approach to calculating mean aerodynamic forces and mean flow fields, which are essential data to investigate urban microclimates.

6. Acknowledgments

For funding this work, the authors would like to thank the Agencia Nacional de Promoción de la Investigación, el Desarrollo Tecnológico y la Innovación (Agencia I+D+i), Argentina, via the projects PICT-2018 N°03252 and PICT-2018 N°02464, Res. N°401-19.

J. Gimenez would like to acknowledge the financial support from the CERCA program of the Generalitat de Catalunya, and from the Spanish Ministry of Economy and Competitiveness through the "Severo Ochoa Programme for Centres of Excellence in R&D" (CEX2018-000797-S).

References

[1] H. Bahi, H. Mastouri, and H. Radoine, "Review of methods for retrieving urban heat islands," *Materials Today: Proceedings*, vol. 27, pp. 3004–3009, 2020.

[2] J. Zou, Y. Yu, J. Liu, J. Niu, K. Chauhan, and C. Lei, "Field measurement of the urban pedestrian level wind turbulence," *Building and Environment*, vol. 194, p. 107713, 2021.

[3] J. Carmeliet, J. Allegrini, P. Moonen, S. Saneinejad, and V. Dorer, "Urban energy and microclimate: wind tunnel experiments and multiscale modeling," in *BUILDING SIMULATION 2013: 13TH INTERNATIONAL CONFERENCE OF THE INTERNATIONAL BUILDING PERFORMANCE SIMULATION ASSOCIATION*, pp. 1014–1021, INT BUILDING PERFORMANCE SIMULATION ASSOC-IBPSA, 2013.

[4] J. Allegrini, "A wind tunnel study on three-dimensional buoyant flows in street canyons with different roof shapes and building lengths," *Building and Environment*, vol. 143, pp. 71–88, 2018.

[5] Y. Toparlar, B. Blocken, B. Maiheu, and G. Van Heijst, "A review on the cfd analysis of urban microclimate," *Renewable and Sustainable Energy Reviews*, vol. 80, pp. 1613–1640, 2017.

[6] B. Blocken, "Les over rans in building simulation for outdoor and indoor applications: A foregone conclusion?," in *Building Simulation*, vol. 11, pp. 821–870, Springer, 2018.

[7] J. Zhong, J. Liu, Y. Zhao, J. Niu, and J. Carmeliet, "Recent advances in modeling turbulent wind flow at pedestrian-level in the built environment," *Architectural intelligence*, vol. 1, no. 1, pp. 1–18, 2022.

[8] J. Franke, A. Hellsten, H. Schlünzen, and B. Carissimo, "Best practice guideline for the cfd simulation of flows in the urban environment," *COST action*, vol. 732, p. 51, 01 2007.

[9] Y. Tominaga, A. Mochida, R. Yoshie, H. Kataoka, T. Nozu, M. Yoshikawa, and T. Shirasawa, "Aij guidelines for practical applications of cfd to pedestrian wind environment around buildings," *Journal of Wind Engineering and Industrial Aerodynamics*, vol. 96, no. 10, pp. 1749 – 1761, 2008.

[10] B. Blocken, "Computational fluid dynamics for urban physics: Importance, scales, possibilities, limitations and ten tips and tricks towards accurate and reliable simulations," *Building and Environment*, vol. 91, pp. 219–245, 2015.

[11] J. M. Gimenez, F. Bre, N. M. Nigro, and V. Fachinotti, "Computational modeling of natural ventilation in low-rise non-rectangular floor-plan buildings," in *Building Simulation*, vol. 11, pp. 1255–1271, Springer, 2018.

[12] G. Vita, Z. Shu, M. Jesson, A. Quinn, H. Hemida, M. Sterling, and C. Baker, "On the assessment of pedestrian distress in urban winds," *Journal of Wind Engineering and Industrial Aerodynamics*, vol. 203, p. 104200, 2020.

[13] A. U. Weerasuriya, X. Zhang, K. T. Tse, C.-H. Liu, and K. C. Kwok, "Rans simulation of near-field dispersion of reactive air pollutants," *Building and Environment*, vol. 207, p. 108553, 2022.

[14] A. Elshaer, G. Bitsuamlak, and A. El Damatty, "Aerodynamic shape optimization of tall buildings using twisting and corner modifications," in *8th International Colloquium on Bluff Body Aerodynamics and Applications Northeastern University*, 2016.

[15] M. A. Mooneghi and R. Kargarmoakhar, "Aerodynamic mitigation and shape optimization of buildings," *Journal of building engineering*, vol. 6, pp. 225–235, 2016.

[16] T.-O. Hågbo and K. E. T. Giljarhus, "Pedestrian wind comfort assessment using computational fluid dynamics simulations with varying number of wind directions," *Frontiers in Built Environment*, vol. 8, 2022.

[17] A. Ricci, I. Kalkman, B. Blocken, M. Burlando, and M. Repetto, "Impact of turbulence models and roughness height in 3d steady rans simulations of wind flow in an urban environment," *Building and Environment*, vol. 171, p. 106617, 2020.

[18] M. Kato and B. E. Launder, "The modeling of turbulent flow around stationary and vibrating square cylinders," in *9th Symp. on Turbulent Shear Flows*, pp. 10–4–1–10–4–6, 1993.

[19] M. Tsuchiya, S. Murakami, A. Mochida, K. Kondo, and Y. Ishida, "Development of a new k-ε model for flow and pressure fields around bluff body," *Journal of Wind Engineering and Industrial Aerodynamics*, vol. 67, pp. 169–182, 1997.

[20] D. Mohotti, K. Wijesooriya, and D. Dias-da Costa, "Comparison of reynolds averaging navier-stokes (rans) turbulent models in predicting wind pressure on tall buildings," *Journal of Building Engineering*, vol. 21, pp. 1–17, 2019.

[21] F. Bre and J. M. Gimenez, "A cloud-based platform to predict wind pressure coefficients on buildings," in *Building simulation*, vol. 15, pp. 1507–1525, Springer, 2022.

[22] M. Cindori, P. Čajić, I. Džijan, F. Juretić, and H. Kozmar, "A comparison of major steady rans approaches to engineering abl simulations," *Journal of Wind Engineering and Industrial Aerodynamics*, vol. 221, p. 104867, 2022.

[23] B. Bhattacharyya and S. K. Dalui, "Experimental and numerical study of wind-pressure distribution on irregular-plan-shaped building," *Journal of structural Engineering*, vol. 146, no. 7, p. 04020137, 2020.

[24] S. Agrawal, J. K. Wong, J. Song, O. Mercan, and P. J. Kushner, "Assessment of the aerodynamic performance of unconventional building shapes using 3d steady rans with sst k-ω turbulence model," *Journal of Wind Engineering and Industrial Aerodynamics*, vol. 225, p. 104988, 2022.

[25] M. Bellegoni, L. Cotteleer, S. K. R. Srikumar, G. Mosca, A. Gambale, L. Tognotti, C. Galletti, and A. Parente, "An extended sst k- ω framework for the rans simulation of the neutral atmospheric boundary layer," *Environmental Modelling & Software*, vol. 160, p. 105583, 2023.

[26] Y. Tominaga, S.-i. Akabayashi, T. Kitahara, and Y. Arinami, "Air flow around isolated gable-roof buildings with different roof pitches: Wind tunnel experiments and cfd simulations," *Building and Environment*, vol. 84, pp. 204–213, 2015.

[27] G. K. Ntinas, X. Shen, Y. Wang, and G. Zhang, "Evaluation of cfd turbulence models for simulating external airflow around varied building roof with wind tunnel experiment," in *Building Simulation*, vol. 11, pp. 115–123, Springer, 2018.

[28] M. Shirzadi, M. Naghashzadegan, and P. A. Mirzaei, "Improving the cfd modelling of cross-ventilation in highly-packed urban areas," *Sustainable cities and society*, vol. 37, pp. 451–465, 2018.

[29] J. Schaefer, S. Hosder, T. West, C. Rumsey, J.-R. Carlson, and W. Kleb, "Uncertainty quantification of turbulence model closure coefficients for transonic wall-bounded flows," *AIAA Journal*, vol. 55, no. 1, pp. 195–213, 2017.

[30] H. Xiao and P. Cinnella, "Quantification of model uncertainty in rans simulations: A review," *Progress in Aerospace Sciences*, vol. 108, pp. 1–31, 2019.

[31] B. Fabritius, *Application of Genetic Algorithms to Problems in Computational Fluid Dynamics*. PhD thesis, University of Exeter, 2014.

[32] M. Tano-Retamales, P. Rubiolo, and O. Doche, *Development of Data-Driven Turbulence Models in OpenFOAM: Application to Liquid Fuel Nuclear Reactors*, pp. 93–108. Cham: Springer International Publishing, 2019.

[33] A. Da Ronch, M. Panzeri, J. Drofelnik, and R. d'Ippolito, "Sensitivity and calibration of turbulence model in the presence of epistemic uncertainties," *CEAS Aeronautical Journal*, vol. 11, no. 1, pp. 33–47, 2020.

[34] M. Yang and Z. Xiao, "Parameter uncertainty quantification for a four-equation transition model using a data assimilation approach," *Renewable Energy*, vol. 158, pp. 215–226, 2020.

[35] D. Romanova, O. Ivanov, V. Trifonov, N. Ginzburg, D. Korovina, B. Ginzburg, N. Koltunov, M. Eglit, and S. Strijhak, "Calibration of the k-ω sst turbulence model for free surface flows on mountain slopes using an experiment," *Fluids*, vol. 7, no. 3, p. 111, 2022.

[36] F. Köhler, J. Munz, and M. Schäfer, "Data-driven augmentation of rans turbulence models for improved prediction of separation in wall-bounded flows," in *AIAA Scitech 2020 Forum*, p. 1586, 2020.

[37] S. Guillas, N. Glover, and L. Malki-Epshtein, "Bayesian calibration of the constants of the k–epsilon turbulence model for a cfd model of street canyon flow," *Computer Methods in Applied Mechanics and Engineering*, vol. 279, pp. 536 – 553, 2014.

[38] M. Shirzadi, P. A. Mirzaei, and Y. Tominaga, "Rans model calibration using stochastic optimization for accuracy improvement of urban airflow cfd modeling," *Journal of Building Engineering*, vol. 32, p. 101756, 2020.

[39] J. M. Gimenez and F. Bre, "Optimization of rans turbulence models using genetic algorithms to improve the prediction of wind pressure coefficients on low-rise buildings," *Journal of Wind Engineering and Industrial Aerodynamics*, vol. 193, p. 103978, 2019.

[40] R. Zhao, S. Liu, J. Liu, N. Jiang, and Q. Chen, "Generalizability evaluation of k-ε models calibrated by using ensemble kalman filtering for urban airflow and airborne contaminant dispersion," *Building and Environment*, vol. 212, p. 108823, 2022.

[41] F. R. Menter, "Two-equation eddy-viscosity turbulence models for engineering applications," *AIAA Journal*, vol. 32, no. 8, pp. 1598–1605, 1994.

[42] F. R. Menter, M. Kuntz, and R. Langtry, "Ten years of industrial experience with the sst turbulence model," *Turbulence, heat and mass transfer*, vol. 4, no. 1, pp. 625–632, 2003.

[43] P. J. Richards and R. P. Hoxey, "Appropriate boundary conditions for computational wind engineering models using the k-ϵ turbulence model," in *Computational Wind Engineering 1* (S. Murakami, ed.), pp. 145–153, Oxford: Elsevier, 1993.

[44] P. Richards and S. Norris, "Appropriate boundary conditions for computational wind engineering models revisited," *Journal of Wind Engineering and Industrial Aerodynamics*, vol. 99, no. 4, pp. 257–266, 2011.

[45] J. Wieringa, "Updating the davenport roughness classification," *Journal of Wind Engineering and Industrial Aerodynamics*, vol. 41, no. 1, pp. 357 – 368, 1992.

[46] D. C. Wilcox, *Turbulence Modeling for CFD*. DCW Industries, 3rd ed., November 2006.

[47] B. Blocken, J. Carmeliet, and T. Stathopoulos, "Cfd evaluation of wind speed conditions in passages between parallel buildings—effect of wall-function roughness modifications for the atmospheric boundary layer flow," *Journal of Wind Engineering and Industrial Aerodynamics*, vol. 95, no. 9-11, pp. 941–962, 2007.

[48] Y. Abu-Zidan, P. Mendis, and T. Gunawardena, "Impact of atmospheric boundary layer inhomogeneity in cfd simulations of tall buildings," *Heliyon*, vol. 6, no. 7, p. e04274, 2020.

[49] D. M. Heargraves and N. G. Wright, "On the use of the k-epsilon model in commercial CFD software to model the neutral atmospheric boundary layer," *Journal of Wind Engineering and Industrial Aerodynamics*, vol. 95, pp. 355–369, 2007.

[50] F. Menter and T. Esch, "Elements of industrial heat transfer predictions," in *16th Brazilian Congress of Mechanical Engineering (COBEM)*, vol. 109, p. 650, 2001.

[51] H. Jasak, "Error analysis and estimation for the finite volume method with applications to fluid flows.," 1996.

[52] J. Gimenez and F. Bre, "Automatic mesh generator for urban computational fluid dynamics simulations," in *Will Cities Survive? Sustainable Architecture Design*, pp. 121–126, PLEA SANTIAGO 2022, 2022. https://plea2022.org/wp-content/uploads/2023/03/PROCEEDINGS-ONSITE-FINAL-MARZO.pdf.

[53] B. Blocken, T. Stathopoulos, J. Carmeliet, and J. L. Hensen, "Application of computational fluid dynamics in building performance simulation for the outdoor environment: an overview," *Journal of Building Performance Simulation*, vol. 4, no. 2, pp. 157–184, 2011.

[54] Y. Quan, Y. Tamura, M. Matsui, S. Cao, and A. Yoshida, "TPU aerodynamic database for low-rise buildings," in *12th International Conference on Wind Engineering*, pp. 2–6, 2007.

[55] J. A. Akubue, "Effects of street geometry on airflow regimes for natural ventilation in three different street configurations in enugu city," in *Different Strategies of Housing Design* (A. B. Çakmaklı, ed.), ch. 2, Rijeka: IntechOpen, 2019.

[56] Y. Tominaga and M. Shirzadi, "Wind tunnel measurement of three-dimensional turbulent flow structures around a building group: Impact of high-rise buildings on pedestrian wind environment," *Building and Environment*, vol. 206, p. 108389, 2021.

[57] Y. Tominaga and M. Shirzadi, "Wind tunnel measurement dataset of 3d turbulent flow around a group of generic buildings with and without a high-rise building," *Data in Brief*, vol. 39, p. 107504, 2021.

[58] S. Murakami, "Overview of turbulence models applied in cwe–1997," *Journal of Wind Engineering and Industrial Aerodynamics*, vol. 74, pp. 1–24, 1998.

[59] Y. Gao and W. K. Chow, "Review on wind-induced air movement around a cube," *Architectural Science Review*, vol. 46, no. 3, pp. 247–257, 2003.

[60] G. Caniot, W. Li, and G. Dupont, "Validations and applications of a cfd tool dedicated to wind assessment in urban areas," in *13th International Conference on Wind Engineering*, 2011.

[61] M. Shirzadi, Y. Tominaga, and P. A. Mirzaei, "Experimental and steady-rans cfd modelling of cross-ventilation in moderately-dense urban areas," *Sustainable Cities and Society*, vol. 52, p. 101849, 2020.

[62] P. A. Mirzaei and J. Carmeliet, "Dynamical computational fluid dynamics modeling of the stochastic wind for application of urban studies," *Building and Environment*, vol. 70, pp. 161–170, 2013.

[63] M. Shirzadi and Y. Tominaga, "Cfd evaluation of mean and turbulent wind characteristics around a high-rise building affected by its surroundings," *Building and Environment*, vol. 225, p. 109637, 2022.

[64] E. R. Shelley, *DATA ANALYSIS AND UNCERTAINTY QUANTIFICATION OF ROOF PRESSURE MEASUREMENTS USING THE NIST AERODYNAMIC DATABASE*. PhD thesis, Cleveland State University, 2022.

[65] M. F. Khaled and A. M. Aly, "Assessing aerodynamic loads on low-rise buildings considering reynolds number and turbulence effects: a review," *Advances in Aerodynamics*, vol. 4, no. 1, pp. 1–33, 2022.